Fuel 325 (2022) 124953

Contents lists available at ScienceDirect

Fuel

journal homepage: www.elsevier.com/locate/fuel

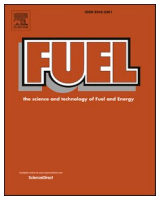

Full Length Article

Water Liberating/Sealing effects on shale gas Extraction: A fully coupled multidomain and multiphysics model

Wai Li [a,*], Jishan Liu [a], Jie Zeng [a], Yee-Kwong Leong [a], Derek Elsworth [b], Jianwei Tian [a]

[a] School of Engineering, The University of Western Australia, Perth, WA 6009, Australia
[b] Department of Energy and Mineral Engineering, G3 Centre and Energy Institute, The Pennsylvania State University, University Park, PA 16802, USA

ARTICLE INFO

Keywords:
Shale gas
Stimulation
Two-phase flow
Flowback
Multidomain
Multiphysics

ABSTRACT

Whether the gas in kerogen is liberated/sealed by water, is a crucial issue for successful shale gas reservoir exploitation. Although this issue has been recognized, no tools are developed to evaluate the impact of this gas liberation/sealing on gas production under in-situ conditions. In this work, a concept named kerogen threshold differential pressure (KTP) is proposed to describe the mass transport influenced by the wettability at the heterogeneous kerogen interface with external/connate water. KTP is defined as a critical pore pressure difference between inside and outside of kerogen pores. It corresponds to the energy barrier needed to remove the liquid film at the kerogen surface so that the gas in kerogen can flow out. Based on this definition, whether kerogen supplies gas to its surroundings or not is controlled by an on/off mechanism which is incorporated into a fully coupled, multidomain, and multiphysics model to simulate gas extraction from stimulated shale reservoirs. Gas flow in kerogen, gas–water-two-phase flowback in inorganic matrix and fractures, shale deformation, and gas sorption are considered in the model. The proposed model is verified against a set of gas production data from the field and the simulation results published by a previous study. Furthermore, a sensitivity analysis is performed to investigate the effects of important influencing factors on gas and water production. The results suggest four main findings: (1) Shale gas production behaviour is dependent on the combination of gas-supplying capabilities of the different components in different domains of shale reservoir. (2) Water influences shale gas extraction in two aspects including two-phase flow and on/off gas supplying mechanism. The former aspect affects the gas flow in inorganic matrix and fractures, while the latter aspect controls the gas liberation from kerogen and thus, the sustainability of gas extraction. (3) The shapes of the gas/water relative permeability curves of different components of shale reservoir are influenced by formation damage and stimulation operation. They mainly affect early-period water production. (4) Gas recovery is enhanced by decreasing KTP, which can be achieved by using appropriate surfactants and/or water-free fracking fluids to alleviate/eliminate formation damage.

1. Introduction

Although shale gas is playing an increasingly more important role in the energy market, accurately predicting gas recovery from shale reservoirs is still a great challenge [1,2]. This is because of the complexities of shale properties, reservoir structure, combined effects of multiple physical processes [3,4], and the interactions between these processes [5,6]. An appropriate numerical computation tool is always highly attractive to the natural gas industry due to its convenience in solving non-linear and coupling equations, treating complex geometries, and presenting evolutions of crucial variables [7]. Obviously, key influencing factors and mechanisms should be incorporated into the numerical computation tool to ensure the reliability and accuracy of simulations. As a non-negligible factor in gas extraction from shale reservoirs, the influence of water (including connate water and invaded work fluids, such as the filtrate of drilling/completion fluids and/or fracking fluids) on shale gas production has been recognized [8]. Previous studies indicate that only a fraction of fracking fluid (typically 10%-50% by volume) can flow back to the surface during shale gas extraction, while the remaining is still in the reservoir due to the strong imbibition effect caused by the high capillary pressure of shale [9,10]. The water in shale reservoirs not only influences the gas mobility in the pores and fractures of inorganic matrix (IM) but also affects the liberation of gas in organic kerogen pockets [11,12]. For the effect of water on

* Corresponding author.
E-mail address: wai.li@research.uwa.edu.au (W. Li).

https://doi.org/10.1016/j.fuel.2022.124953
Received 16 December 2021; Received in revised form 12 June 2022; Accepted 16 June 2022
Available online 23 June 2022

gas mobility, gas–water-two-phase flowback models have been comprehensively employed to describe and quantify the impact of water on effective porosity, relative permeability, and the resultant two-phase flowback process [13,14]. Briefly speaking, the saturations of gas and water are used to express the fractions of pore volume occupied by these two phases, while the relative permeabilities reflect the curtailing effect of water on the phase permeability of gas [15]. These models based on the corrections of porosity and permeability are included in the governing equations of mass transfer to simulate the gas–water-two-phase flow process [16]. However, the scientific knowledge and deep understanding of the liberation process of gas from kerogen pockets influenced by water are still very limited and often ignored in modelling and simulation. Since a considerable amount of shale gas is originally stored in kerogen (20%-85% of the total reserve, according to Curtis [17]), it is necessary to develop reliable physical and mathematical models which include the mechanism of the gas liberation process from kerogen pockets influenced by water, and then incorporate these models into the reservoir simulation tools so that the accurate evaluation of shale gas production with water effects can be achieved.

In previous studies, the effect of water on the gas supply from the organic matrix (e.g., kerogen) of unconventional gas reservoirs is often simply treated as an empirical modification of the gas adsorption capacity to express the fact that the amount of gas desorbed from water-containing reservoirs is smaller than that desorbed from the reservoirs without water [18,19]. The modified gas adsorption capacity is related to the water content [20,21]. However, this approach ignores some important mechanisms. In the real kerogen pockets, the organic pore size is usually nanometer-level and hydrophobic, leading to a very high capillary pressure preventing external water from invading the organic pores. Thus, before shale gas extraction, the water tends to exist as a film at the heterogeneous interface between kerogen and inorganic matter instead of being in the pores of kerogen pockets [1]. In consequence, when shale gas extraction is performed, this water film, like a seal, may prevent the gas originally in kerogen from flowing out. During shale gas extraction, the water film distribution at the heterogeneous interface changes with the pore pressure depletion in the IM wrapping the kerogen pockets, so a kerogen pocket is sometimes opened to supply gas while sometimes closed. That is, the sealing effect of the water film on the gas supply of kerogen pockets varies with production time. This mechanism has been demonstrated by Lee et al. [1]. By using molecular modelling and mesoscale simulation, they proved that whether the water film seals the kerogen pockets or not is dependent on the system energy. More specifically, there is an activation energy barrier (i.e., a critical Gibbs free energy change) for kerogen with water film at the heterogeneous interface between kerogen and IM. If the gas energy in a kerogen pocket with water film is sufficiently high, the pocket can supply gas to the surrounding inorganic pores and fractures. Otherwise, the kerogen pocket with water film will be closed, the gas stored in this pocket has no contribution to the gas transport in the reservoir. This mechanism, referred to as the "on/off gas-supplying mechanism" in this work, dynamically affects the gas production from shale reservoirs.

Although this on/off mechanism of gas supply from the kerogen pockets with water film has been recognized by researchers, no computation tools are developed to evaluate the impact of this mechanism on gas production under in-situ conditions because there are several technical difficulties as follows: (1) It is challenging to incorporate this mechanism into the existing models which are based on the evolution of reservoir pore pressure instead of energy change. As mentioned above, Lee et al. describe this mechanism as a process controlled by the system energy [1]. However, the exact energy distribution in the reservoir is not easy to determine and seldom used in reservoir modelling and simulation. In contrast, pore pressure is the most commonly used crucial variable to describe the gas production process because there are a variety of existing models and formulas associating the evolutions of reservoir properties with pore pressure. Therefore, a pressure-based expression (both in physics and in math) of the mechanism of gas supply from kerogen is needed. (2) Gas-water-two-phase flowback should be combined with the on/off mechanism to integrate the different effects caused by water on the gas storage and transport during shale gas recovery [11,15]. (3) Mechanical deformation of shale during gas extraction should be incorporated into the model to reflect the stress dependence of porosity and absolute permeability [22]. (4) Various porous media at different scales should be individually incorporated into the model to reflect the high heterogeneity of shale reservoirs. These porous media, including primary hydraulic fracture (HF), natural fracture system (NA), inorganic matrix (IM), and kerogen, have different porosity and permeability. Moreover, the gas flow in these media obeys different flow regimes, influencing the apparent permeabilities [23,24]. (5) After hydraulically fracking, the stimulated shale reservoir is divided into three different domains including HF, stimulated reservoir domain (SRD), and non-stimulated reservoir domain (NSRD) [4]. These domains have distinct properties and thus, different property evolutions. This multidomain effect, discussed by the previous studies [22,25], should also be taken into consideration.

In this work, a concept of kerogen threshold differential pressure (*KTP*) is proposed to describe the on/off mechanism of gas supply from kerogen with water film at the heterogeneous interface. After that, a fully coupled, multidomain, multiphysics, two-phase flowback model is built to comprehensively incorporate the effects of water (including the on/off gas-supplying mechanism and gas–water-two-phase flowback) into the simulation of the whole process of shale gas extraction. The proposed model is then verified against a set of gas production data from the field and the simulation results of water production published by a previous study. Furthermore, a sensitivity analysis is performed to comprehensively investigate the effects of important influencing factors on gas and water production. The significance of the on/off gas-supplying mechanism for engineering practice is especially discussed.

2. Conceptual model

In this section, a conceptual model is detailed to establish the basic framework of the multidomain, multiphysics, two-phase flowback model. As a major innovation of this work, the concept of kerogen threshold differential pressure (*KTP*) is firstly proposed. A multiscale model is then introduced to characterize the heterogeneous shale. Subsequently, the different domains are conceptually divided to define the multidomain characteristic of the stimulated shale reservoir. The effects of flow regimes on gas flow in the pores with different scales are also claimed. Besides, the flow sequence is proposed to link the mass transfer occurring in these porous media and domains.

2.1. Kerogen threshold differential pressure (KTP) and on/off gas-supplying mechanism

As the key concept of the on/off gas-supplying mechanism, kerogen threshold deferential pressure (*KTP*) is defined as a critical pore pressure difference between inside and outside of kerogen pores. An illustration describing the concept of *KTP* is shown in Fig. 1. At the heterogeneous interface between kerogen and inorganic matrix (IM), some organic nanopores [see Fig. 1, **inset (a)**] are opened to release their internal gas. The released gas comes from the original free gas and the desorbed gas with the pore pressure depletion in kerogen. In contrast, other organic nanopores are sealed by a water film, so the gas stored in these kerogen pores cannot flow out. The sealing water may be connate water or invaded external water (e.g., fracking fluids, drilling/completion fluid filtrate, etc.). Furthermore, the on/off states of these organic nanopores may change with time because they are controlled by the varying local difference between kerogen pore pressure (p_k, this pressure denotes the gas pressure in kerogen) and IM pore pressure (p_m, this pressure denotes the average fluid pressure of gas and water in IM). During shale gas extraction, the p_m continuously decreases, which increases the value of the differential pressure ($p_k - p_m$). When ($p_k - p_m$) is higher than *KTP*, the

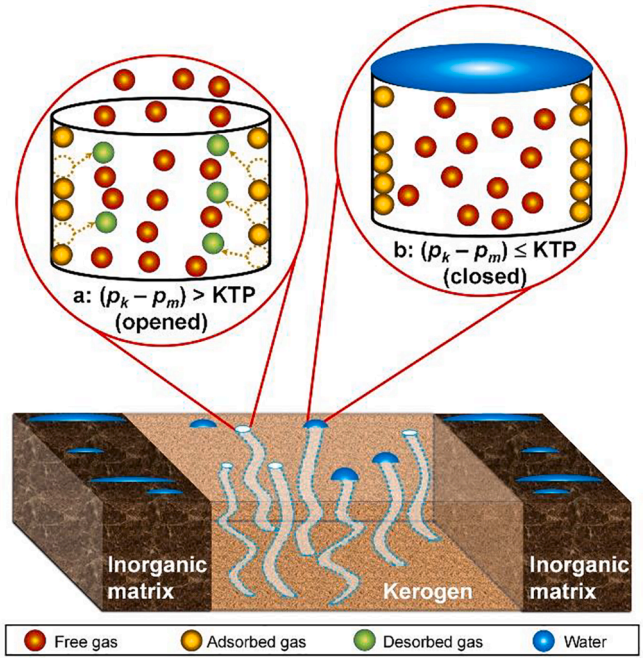

Fig. 1. On/off gas-supplying mechanism of gas liberation from kerogen. (a) An opened nanopore of kerogen without water film [$(p_k - p_m) > KTP$]. (b) A nanopore of kerogen sealed by a water film [$(p_k - p_m) \leq KTP$].

organic nanopore will open to supply gas. This gas supply leads to the reduction of p_k, which decreases the value of $(p_k - p_m)$. Subsequently, $(p_k - p_m)$ may become lower than KTP again, and the nanopore is shut down to stop supplying gas. Therefore, we have the following criterion to determine the on/off state of kerogen:

$$\begin{cases} if\ p_k - p_m > KTP, \text{ kerogen is opened} \\ if\ p_k - p_m \leq KTP, \text{ kerogen is closed} \end{cases} \quad (1)$$

The essence of KTP is the pressure energy difference between the inside and the outside of the kerogen pores with water film. It is a pressure-form expression of the concept of "activation energy barrier" to remove the liquid film sealing the kerogen pores so that the gas in kerogen can flow out [1].

2.2. Multi-scale model and domain division

A hierarchical, multi-scale model is used to characterize various pores and fractures with different scales so that the heterogeneity of the hydraulically fractured shale reservoir can be reflected, as shown in Fig. 2. More specifically, the multi-scale model includes the following media: (1) Kerogen [Fig. 2**(a)**]. Kerogen pores are deemed as a bundle of tortuous organic capillary tubes with nano-meter-level pore size. (2) Inorganic matrix [IM, see Fig. 2**(b)**]. IM is considered as an inorganic continuum having tortuous tube-shaped pores of which size is larger than kerogen pores. Both kerogen and IM are very tight and have ultra-low permeability, and they occupy the most volume of the bulk shale. (3) Natural fractures network [NA, see Fig. 2 **(c1) and (c2)**]. NA is deemed as an inorganic continuum with significantly higher porosity and permeability than those of kerogen and IM, representing the natural fractures network throughout the bulk shale. NA has planar fractures with an average aperture ranging from sub-micrometer to micrometer level, and it accounts for a small volumetric fraction of the bulk shale. (4) Primary hydraulic fracture [HF, see Fig. 2**(d)**]. HF is simplified as a 1-D, discrete, fractured inorganic medium with a millimeter-level aperture. As continua, kerogen, IM, and NA constitute a triple-porosity-triple-permeability system to describe the bulk shale, while a set of HFs are discretely specified and embedded in the bulk shale. Thus, the four porous media with different pore scales construct the hydraulically fractured shale gas reservoir.

Moreover, as the consequence of hydraulic fracking, NA can be further divided into two domains: NA-SRD [natural fractures network in the stimulated reservoir domain, see Fig. 2**(c1)**] and NA-NSRD [natural fractures network in the non-stimulated reservoir domain, see Fig. 2**(c2)**]. NA-SRD represents the natural fractures network near-HF zone containing many secondary hydraulic fractures. It has higher porosity, absolute permeability, as well as a lower bulk volumetric modulus than those of NA-NSRD which has all the original properties of NA. For kerogen and IM, they have identical properties in the whole reservoir. That is, SRD and NSRD have different NA properties while having the same kerogen and IM properties (unless stated otherwise). Thus, a hydraulically fractured shale gas reservoir is abstracted as an assembly of four media (kerogen, IM, NA, and HF) with three domains (SRD, NSRD, and HF).

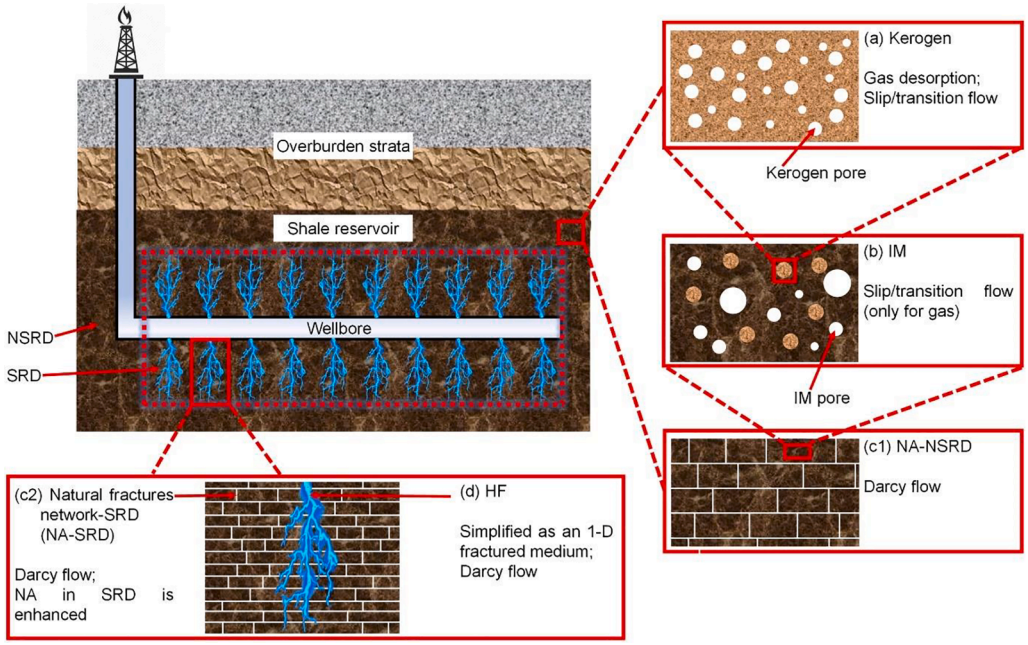

Fig. 2. Illustration of a producing shale gas reservoir with multi-scale porous media and multiple domains: (a) Kerogen; (b) IM; (c1) NA-NSRD; (c2) NA-SRD; (d) HF.

The storage forms and flow types of fluids in the four media of the stimulated shale reservoir are different. Gas stored in kerogen pores has the forms of free gas and adsorbed gas, and there is no water stored in the internal kerogen. In contrast, Gas and water coexist in IM, NA, and HF because of the imbibition effect induced by the hydrophilic feature of the inorganic surfaces of these media. Therefore, single gas flow occurs in kerogen, while gas–water-two-phase flow occurs in IM, NA, and HF. In addition, the gas stored in IM, NA, and HF is only in the form of free gas because gas sorption in these inorganic media can be ignored [23,26].

Another worth noting issue is that the initial water saturations in the different media and domains are also different. Before gas production, as a direct consequence of fracking fluid invasion, HF contains a large amount of water and a small fraction of gas. NA-SRD also has a considerable water saturation because the fracking fluid tends to enter the secondary hydraulic fractures. However, the water saturation of NA-NSRD is much lower than that in NA-SRD because NSRD is not enhanced by the fracking treatment. Differed from NA, although IM has a certain of water saturation originated from the connate water and the imbibition effect, the water mobility in IM is low because of the high capillary resistance to water flow in the micro/nanopores of IM. There is no water in the internal kerogen except the water film at the heterogeneous interface between kerogen and IM. The volume of the water film is included in IM water saturation.

2.3. Gas flow regimes and sequence

Due to the extremely small pore sizes of kerogen and IM, the gas flow regimes in these two media range from slip flow to transition flow, which is dependent on the orders of magnitude of the Knudsen numbers in these two media [27,28]. As a result, the apparent permeability of gas in kerogen and IM should be corrected to include the flow regime effect. In contrast, the gas flow regime effect can be ignored in NA and HF due to their relatively large pore sizes [26,29]. For water flow, there is no flow regime effect in all the media and domains [11,22,30]. By setting corrected apparent permeability formulas (see **Sections 3.2 and 3.3**), the effects of flow regimes on gas flow in kerogen and IM can be reflected.

A hierarchical, multidomain flow sequence is used to describe the mass transfer in a producing shale reservoir stimulated by hydraulic fracking treatment. As displayed in Fig. 3, at the beginning of gas production, gas and water in HF rapidly flow out because of the difference between the initial reservoir pressure and the bottom-hole pressure (*BHP*, see the Flow stage 1 in Fig. 3). In consequence, the pore pressure in the HFs becomes much lower than that in the NA, inducing the gas and water in the NA to flow into the HFs (Flow stage 2 in Fig. 3). The reduced pore pressure in the NA then promotes the gas and water in IM to flow into NA (Flow stage 3 in Fig. 3). After that, the decreased pore pressure in IM forces the kerogen to supply gas under the control of the on/off mechanism (Flow stage 4 in Fig. 3). Besides, the pore pressure gradient between NA-SRD and NA-NSRD also leads to the flow and re-distribution of gas and water, which reflects the fact that NA is the main channel of gas–water flow in the whole shale reservoir. This hierarchical, multidomain flow sequence has been successfully used in some previous works to express the gas transport process in hydraulically fractured shale gas reservoirs [4,22]. Nevertheless, the previous models are two-porosity-two-permeability (kerogen + IM) systems, which cannot finely describe the peculiar evolution in the natural fractures network. Some other previous studies [26,31,32] used the triple-porosity (kerogen + IM + NA) system to model and simulate shale gas extraction, but their models neither include the explicitly specified HFs nor differentiate the SRD and the NSRD, ignoring the multidomain effects. Here, we extend the hierarchical, multidomain flow sequence to a triple-porosity, multidomain system along with explicitly specified HFs for gas–water-two-phase flow so that the complex mass transfer in different components and domains of the shale reservoir can be accurately modelled and simulated.

3. Mathematical model

In this section, a mechanical balance equation is first given to fully couple the stress-deformation relationship in the whole shale reservoir. After that, the governing equations describing the mass transport in different media and domains, as well as the mass exchange between these medium and domains, are derived based on the following assumptions: (1) Kerogen, IM, and NA are isotropic and linear-elastic continua; (2) Strains are infinitesimal; (3) Shale gas extraction is an isothermal process; (4) Kerogen is saturated by methane in the initial state; (5) Gas-water-two-phase flow occurs in IM, NA, and HFs, while single-phase flow (gas flow) occurs in kerogen; (6) There is no mass exchange between gas and water phases; (7) The gravitational effect is ignored.

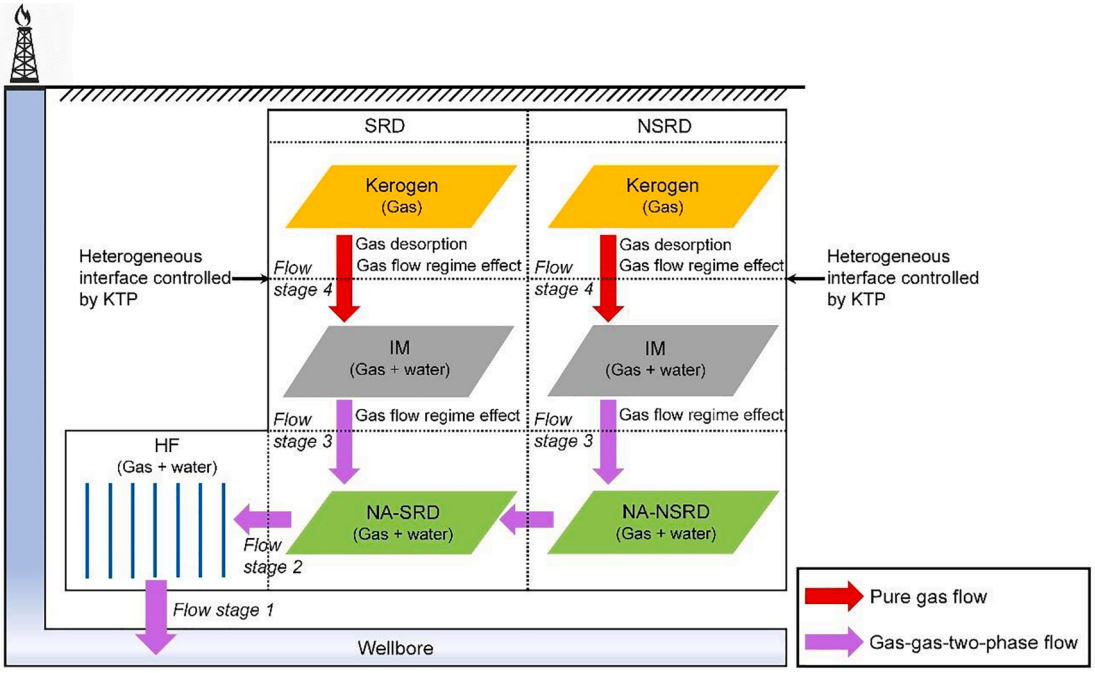

Fig. 3. Hierarchical multidomain flow sequence in a hydraulically fractured shale gas reservoir.

3.1. Mechanical coupling equations

Based on Biot's theory in poroelasticity and the triple-porosity assumption, the stress–strain relationship of the entire shale reservoir can be derived as the following form [33,34,35]:

$$\varepsilon_{ij}=\frac{(1+\upsilon)}{3K(1-2\upsilon)}\sigma_{ij}-\frac{\upsilon}{3K(1-2\upsilon)}\sigma_{kk}\delta_{ij}+\frac{\alpha_k p_k}{3K}\delta_{ij}+\frac{\alpha_m p_m}{3K}\delta_{ij}+\frac{\alpha_{na} p_{na}}{3K}\delta_{ij}+\frac{\varepsilon_s}{3}\delta_{ij} \tag{2}$$

where ε_{ij} is the component of the total strain tensor; υ is the Poisson's ratio of shale; K represents the bulk volumetric modulus of shale; the total stress $\sigma_{kk}=\sigma_{11}+\sigma_{22}+\sigma_{33}$, where σ_{11}, σ_{22} and σ_{33} are the principal stresses in the three axial directions of the spatial coordinate system, respectively; δ_{ij} denotes the Kronecker delta with 1 for $i=j$ and 0 for $i\neq j$. ε_s denotes the sorption-induced volumetric strain; p_k, p_m, and p_{na} denote the pore pressures of kerogen, IM, and NA, respectively. In kerogen (containing only gas), p_k equals the gas pressure (p_{gk}); while in IM, NA, and HF (containing both gas and water), the pore pressures are the average fluid pressures of gas and water [36,37]:

$$\begin{cases} p_k=p_{gk} \\ p_m=S_{gm}p_{gm}+S_{wm}p_{wm} \\ p_{na}=S_{gna}p_{gna}+S_{wna}p_{wna} \\ p_f=S_{gf}p_{gf}+S_{wf}p_{wf} \end{cases} \tag{3}$$

where p_f is the pore pressure in HF; p_{gm}, p_{gna}, and p_{gf} are the gas pressures in IM, NA, and HF; p_{wm}, p_{wna}, and p_{wf} are the water pressures in IM, NA, and HF; S_{gm}, S_{gna}, and S_{gf} are the gas saturations in IM, NA, and HF; S_{wm}, S_{wna}, and S_{wf} are the water saturations in IM, NA, and HF, respectively.

In Eq., K can be defined as a volumetric-weighted average quantity of the individual volumetric moduli of kerogen (K_k), IM (K_m), and NA (K_{na}) according to the studies proposed by Berryman [38] and Cao et al. [23]:

$$\frac{1}{K}=\frac{\eta_k}{K_k}+\frac{\eta_m}{K_m}+\frac{\eta_{na}}{K_{na}} \tag{4}$$

where η_k, η_m, and η_{na} are the volumetric fraction of kerogen, IM, and NA in the bulk shale. $\eta_k+\eta_m+\eta_{na}=1$. Similarly, υ is a volumetric-weighted average quantity of the individual Poisson's ratios of kerogen (υ_k), IM (υ_m), and NA (υ_{na}):

$$\upsilon=\eta_k\upsilon_k+\eta_m\upsilon_m+\eta_{na}\upsilon_{na} \tag{5}$$

On the other hand, α_k, α_m, and α_{na} in Eq. are the effective Biot coefficients of kerogen, IM, and NA, respectively. They are determined according to the method proposed by the studies of Mehrabian and Abousleiman [39] and Cao et al. [23]:

$$\begin{cases} \alpha_k=\dfrac{\eta_k K\alpha_k^*}{K_k} \\ \alpha_m=\dfrac{\eta_m K\alpha_m^*}{K_m} \\ \alpha_{na}=\dfrac{\eta_{na} K\alpha_{na}^*}{K_{na}} \end{cases} \tag{6}$$

whereα_k^*,α_m^*, and α_{na}^* are the individual Biot coefficients of kerogen, IM, and NA, respectively.

ε_s can be obtained by using the Langmuir-type relation:

$$\varepsilon_s=\frac{\varepsilon_L p_k}{p_k+P_L} \tag{7}$$

where ε_L and P_L are the Langmuir sorption strain and Langmuir pressure constants of shale, respectively.

The terms on the right hand of Eq. represent the different contributions to the total strain of shale. The first and the second terms represent the strains induced by the mechanical stress tensor in the shear- and normal- directions, respectively. The third, the fourth and the fifth terms denote the strains caused by the pore pressure evolutions in kerogen, IM, and NA, respectively. The sixth term is the contribution of sorption-induced strain on the total strain tensor.

Furthermore, the strain tensor ε_{ij} can also be expressed as displacements [33,34]:

$$\varepsilon_{ij}=\frac{1}{2}\left(u_{i,j}+u_{j,i}\right) \tag{8}$$

where u_i is the displacement in the i direction and $u_{i,j}$ represents the first-order partial derivative of displacement.

The force equilibrium equation neglecting inertial effects is given as:

$$\sigma_{ij,j}+f_i=0 \tag{9}$$

where σ_{ij} is the stress tensor and f_i is the body force.

Combining Eqs., and yields the Navier-type equation as the final mechanical constitutive relationship:

$$\frac{3K(1-2\upsilon)}{2(1+\upsilon)}u_{i,kk}+\frac{3K}{2(1+\upsilon)}u_{k,ki}-\alpha_k p_{k,i}-\alpha_m p_{m,i}-\alpha_{na}p_{na,i}-\frac{K\varepsilon_L P_L}{(p_k+P_L)^2}p_{k,i}+f_i=0 \tag{10}$$

As mentioned above, the displacement can be converted to the strain tensor ε_{ij}, while ε_{ij} can be directly converted to the stress tensor σ_{ij} based on the linear-elasticity assumption: $\sigma_{ij}=K\varepsilon_{ij}$. Therefore, according to the pressure distribution, we can first numerically solve Eq. (10) to obtain the displacement field, then obtain the strain/stress distribution.

3.2. Gas transport in kerogen

3.2.1. Governing equation of kerogen

Based on the mass conservation law, the governing equation for gas transport in kerogen can be derived as the following form [4,25]:

$$\frac{\partial\left(\rho_{gk}\phi_{k,stress}+\rho_a\rho_s V_{ads}\right)}{\partial t}+\nabla\cdot\left(-\rho_{gk}\frac{k_{kapp}}{\mu_g}\nabla p_{gk}\right)=-Q_{k-m} \tag{11}$$

where ρ_{gk} is the gas density in kerogen, computed according to the real gas equation of state (see **Appendix 3A**); $\phi_{k,stress}$ is the stress-dependent kerogen porosity; ρ_a is the methane density under the standard condition, 0.717 kg/m^3; ρ_s is the shale density; V_{ads} is the adsorption volume per unit of shale mass as standard gas volume; k_{kapp} is the apparent kerogen permeability influenced by stress dependence and gas flow regime; μ_g is the gas viscosity; -$Q_{k\text{-}m}$ is the mass sink term of kerogen supplying gas to IM. The first term on the left hand of Eq. is the storage term including the free gas ($\rho_{gk}\phi_{k,stress}$) and the adsorbed gas ($\rho_a\rho_s V_{ads}$), while the second term on the left hand is the flow term.

3.2.2. Porosity model, apparent permeability model, and adsorption volume

In Eq., $\phi_{k,stress}$ is determined by the stress-dependent porosity model proposed by Cui and Bustin based on the tri-axial stress condition [40]. This model has been widely used in shale reservoir modelling [4,23]:

$$\phi_{k,stress}=\phi_{k0}\exp\{-C_k[(\overline{\sigma}-\overline{\sigma_0})-\alpha_k(p_k-p_{k0})]\} \tag{12}$$

where ϕ_{k0} is the initial kerogen porosity; $\overline{\sigma}$ is the mean total stress numerically solved by the mechanical coupling equation; $\overline{\sigma_0}$ is the initial mean total stress solved by the mechanical coupling equation based on the initial and boundary conditions; p_{k0} is the initial pore pressure in kerogen; C_k is the pore compressibility of kerogen, defined as $C_k=\alpha_k/(\phi_{k0}K_k)$ [40,41]. The term $[(\overline{\sigma}-\overline{\sigma_0})-\alpha_k(p_k-p_{k0})]$ represents the change of effective stress of kerogen taking the initial effective stress of kerogen as the reference.

Considering the gas flow regime, the apparent kerogen permeability is expressed as:

$$k_{kapp}=k_{k,stress}\frac{f(Kn_k)}{f(Kn_{k0})} \tag{13}$$

where $k_{k,stress}$ is the stress-dependent kerogen permeability; $f(Kn_k)$ is a permeability enhancement function generalizing the effect of the flow

regime (ranging from viscous flow to slip flow and transition flow); Kn_k is the Knudsen number in kerogen; Kn_{k0} is the initial Knudsen number in kerogen. $k_{k,stress}$ is determined by combining Eq. and the cubic law [42]:

$$k_{k,stress} = k_{k0}\exp\{-3C_k[(\overline{\sigma}-\overline{\sigma_0})-\alpha_k(p_k-p_{k0})]\} \quad (14)$$

where k_{k0} is the initial apparent permeability of kerogen.

The expression of $f(Kn_k)$ and a general method of calculating the Knudsen numbers in kerogen and IM are detailed in **Appendix 3B**.

The adsorption volume V_{ads} in Eq. is obtained by using Langmuir's isotherm:

$$V_{ads} = \frac{V_L p_k}{P_L + p_k} \quad (15)$$

where V_L is the Langmuir volume constant of shale.

3.2.3. Mass sink term

The mass sink term $Q_{k\text{-}m}$ is determined by the following equation based on the theory proposed by Kazemi et al. [43] and the on/off mechanism for kerogen supplying gas to IM introduced in **Section 2.1**:

$$Q_{k-m} = \frac{D_{k-m}\rho_{gk}k_{kapp}}{\mu_g}(p_k - p_m)\left[S_{gm} + S_{wm}\cdot switch(p_k, p_m)\right] \quad (16)$$

where $D_{k\text{-}m}$ is a shape factor related to the specific interfacial area of the kerogen pockets. For example, for spherical kerogen pockets, $D_{k\text{-}m} = 3/R_k{}^2$, where R_k is the mean radius of the kerogen pockets [4,43]. *switch* (p_k, p_m) is a control function reflecting the on/off gas-supplying mechanism of the kerogen with water film, which is determined by comparing the values of differential pressure ($p_k - p_m$) and *KTP* according to Eq.:

$$switch(p_k, p_m) = \begin{cases} 1, & if\ p_k - p_m > KTP \\ 0, & if\ p_k - p_m \le KTP \end{cases} \quad (17)$$

The term [$S_{gm} + S_{wm}$·*switch*(p_k, p_m)] in Eq. means that the gas supplied by kerogen is the sum of two parts: one (S_{gm}) is from the kerogen without water film, the other is from the opened/closed kerogen with water film [S_{wm}·*switch*(p_k, p_m)]. So the key issue here is to determine the exact expression of *KTP*. The detailed derivation is presented below.

3.2.4. Derivation of KTP expression for kerogen with water film

When the differential pressure between the pore pressures in IM and in a kerogen pocket with water film is not higher than *KTP*, i.e., $0 < p_k - p_m \le KTP$ (this is caused by the shale gas depletion in IM), the gas in kerogen is not capable of flowing out from the kerogen pocket but is confined by a spherical cap which is full of gas at the heterogeneous interface between kerogen and IM. Only if $p_k - p_m > KTP$ (this is caused by the further gas pressure depletion in IM with the gas production), can the confined gas in kerogen get rid of the restriction of the spherical cap and flow into IM. This criterion describes how the energy of the gas in kerogen exceeds the activation energy barrier (ΔG^*, Gibbs free energy change) needed to break the spherical cap, as illustrated in Fig. 4. This mechanism has been demonstrated by the study of Lee et al. [1] based on a molecular dynamics simulation. Here, our main objective is to translate ΔG^* into a critical value of differential pressure between kerogen and IM, i.e., *KTP*. As seen in Fig. 4, in a typical quasi-equilibrium state ($p_k - p_m \le KTP$), the shape of the spherical cap is determined by an effective contact angle (θ_{eff}) and a contact area (A^*). A^* is defined as the contact area of the single spherical cap at the interface: $A^* = \pi d^{*2}/4$, where d^* is the diameter of the single spherical cap (see Fig. 4). θ_{eff} can be calculated by the Cassie–Baxter equation presenting that the cosine value of the effective contact angle is a linear combination of the cosine values of the contact angles on the kerogen solid (θ_{solid} can be measured experimentally) and on the pore zone (where $\theta_{pore} = 0°$) [44]:

$$\theta_{eff} = \arccos\left[\phi_{k,stress} + (1-\phi_{k,stress})\cos\theta_{solid}\right] \quad (18)$$

By conducting a mesoscale analysis of the spherical cap shape, Lee et al. [1] demonstrated that ΔG^* for gas liberation has the following

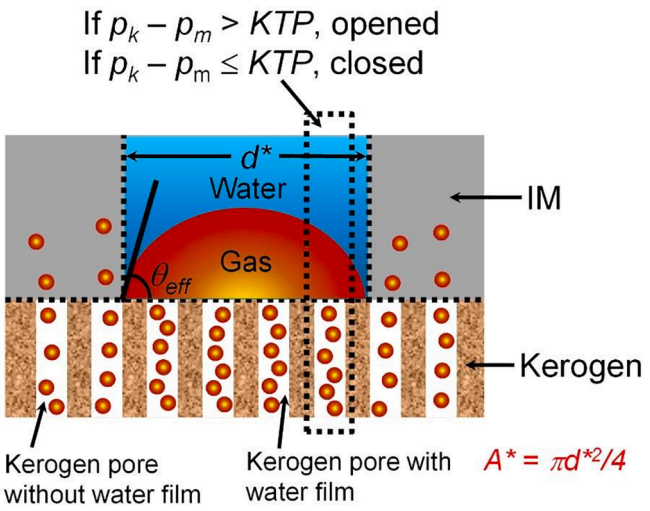

Fig. 4. Geometry of the methane spherical cap with an effective contact angle and a contact area at the interface between IM and kerogen with water film. θ_{eff} is the effective contact angle calculated by using the Cassie–Baxter equation; A^* is the contact area of the spherical cap at the interface; d^* is the diameter of the spherical cap.

relationship with θ_{eff}, gas–water interfacial tension ($\gamma_{g\text{-}w}$), and Kelvin radius (R^*):

$$\Delta G^* = \kappa(\theta_{eff})\gamma_{g-w}R^* \quad (19)$$

where $\kappa(\theta_{eff})$ is a geometrical factor. When the θ_{eff} is not very large, the expression of $\kappa(\theta_{eff})$ is given by the following expression [1,45–49]:

$$\kappa(\theta_{eff}) = \frac{8}{27}\pi\theta_{eff}^4 \quad (20)$$

R^* is defined by the ratio of $\gamma_{g\text{-}w}$ and ($p_k - p_m$):

$$R^* = \frac{\gamma_{g-w}}{p_k - p_m} \quad (21)$$

Combining Eqs., and gives an expression of ΔG^*:

$$\Delta G^* = \frac{8\pi\gamma_{g-w}^3\theta_{eff}^4}{27(p_k - p_m)^2} \quad (22)$$

Eq. relates the activation energy barrier to the pore pressure difference between inside and outside of kerogen pores.

On the other hand, we consider the activation energy barrier from the perspective of surface free energy. When the gas is sealed in the kerogen pocket by the water film, the kerogen surface is covered by the water film. Once the gas is liberated, the water film is removed from the kerogen surface. Thus, the heterogeneous interface experiences a process of the gas displacing the water film. The initial state of kerogen with water film is illustrated in Figs. 3-5(a), while the critical state that the gas in kerogen with water film is about to be liberated is depicted in Figs. 3-5(b). Obviously, the gas liberation is equivalent can be deemed as "the gas spreading on the kerogen surface". According to previously published principles in surface physical chemistry [1,50,51], we can directly obtain the expression of the surface Gibbs free energy change of this spreading process (ΔG^*_{surf}):

$$\Delta G^*_{surf} = -A^* S_{sp}(1-\phi_{k,stress}) \quad (23)$$

where S_{sp} is the spreading parameter defined as:

$$S_{sp} = \gamma_{k-g} - \gamma_{g-w} - \gamma_{k-w} \quad (24)$$

where $\gamma_{k\text{-}g}$ and $\gamma_{k\text{-}w}$ are the solid–gas interfacial tension and solid-water interfacial tension, respectively. In practical laboratory tests, both $\gamma_{k\text{-}g}$ and $\gamma_{k\text{-}w}$ are difficult to obtain. Therefore, we must convert the

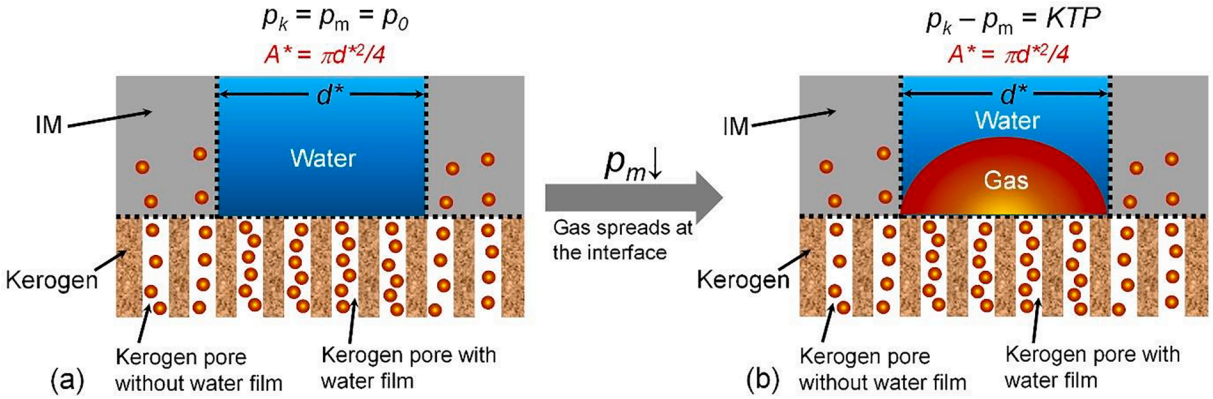

Fig. 5. Gas liberation of the kerogen with water film can be considered as a spreading process of gas on the heterogeneous interface. (a) The initial state of kerogen with water film. (b) The critical state in which the gas in kerogen with water film is about to be liberated.

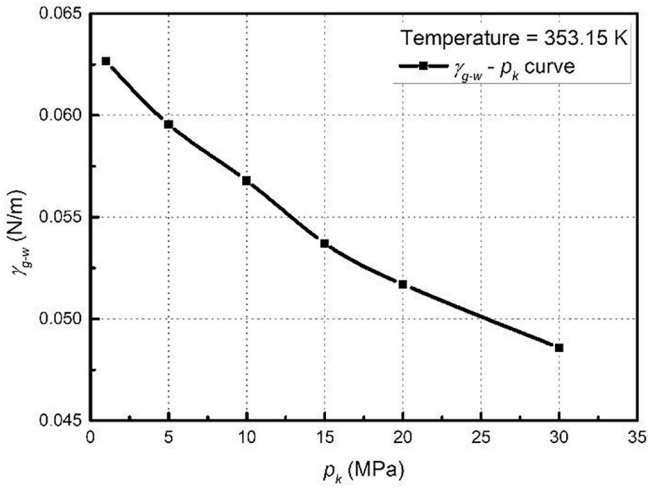

Fig. 6. Values of methane-water interfacial tension under different gas pressures (Temperature = 353.15 K, according to the data provided by Ren et al. [55]).

expression of S_{sp} into a form without $\gamma_{k\text{-}g}$ and $\gamma_{k\text{-}w}$. According to the classic Young-Laplace equation [50], the interfacial tensions $\gamma_{k\text{-}g}$, $\gamma_{k\text{-}w}$, and $\gamma_{g\text{-}w}$ obey the following relation:

$$\gamma_{g-w}\cos\theta_{eff} = \gamma_{k-g} - \gamma_{k-w} \tag{25}$$

Combining Eqs. and yields an expression of S_{sp} without $\gamma_{k\text{-}g}$ and $\gamma_{k\text{-}w}$:

$$S_{sp} = \gamma_{g-w}\left(\cos\theta_{eff} - 1\right) \tag{26}$$

Eq. indicates that S_{sp} always has a negative value, implying the gas-confined state (i.e., gas is trapped in kerogen by a water film at the heterogeneous interface of kerogen) is thermodynamically stable [1]. To release the gas sealed in kerogen by the water film, the value of $(p_k - p_m)$ should be increased by the depletion of p_m to enhance the potential energy of the gas in kerogen and climb the activation energy barrier. Combining Eqs. and gives a new expression ofΔG^*_{surf}:

$$\Delta G^*_{surf} = -A^*\gamma_{g-w}\left(\cos\theta_{eff} - 1\right)\left(1 - \phi_{k,stress}\right) \tag{27}$$

Lee et al. [1] have demonstrated that the gas liberation process and the gas spreading process at the heterogeneous interface of kerogen are thermodynamically equivalent. Therefore, we have the following equation:

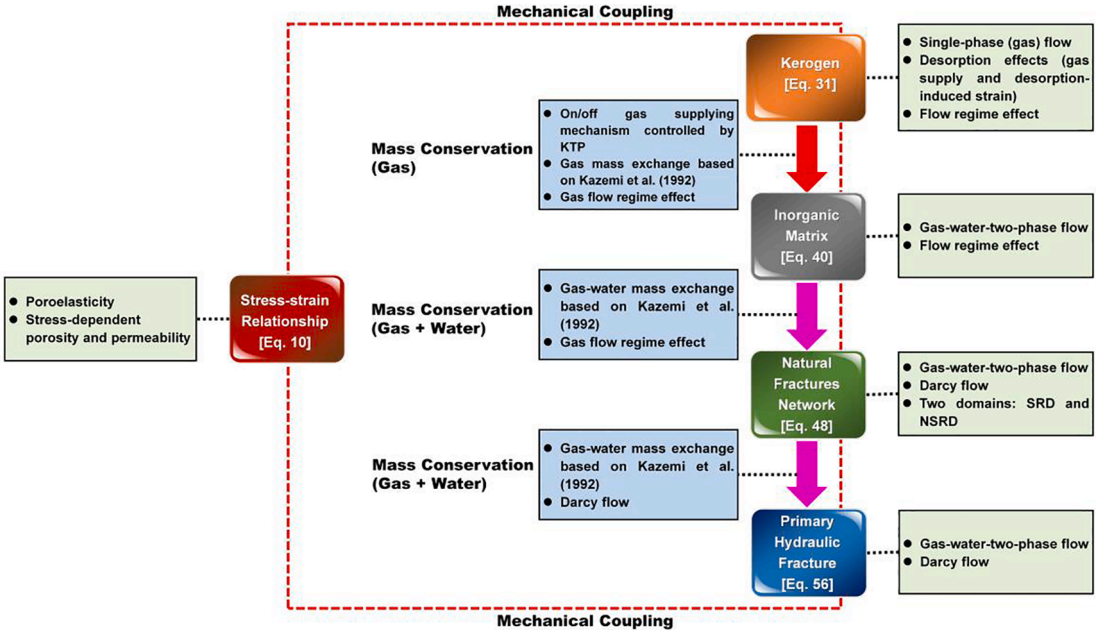

Fig. 7. Relationship and interactions between different porous media and physical processes in a stimulated shale gas reservoir.

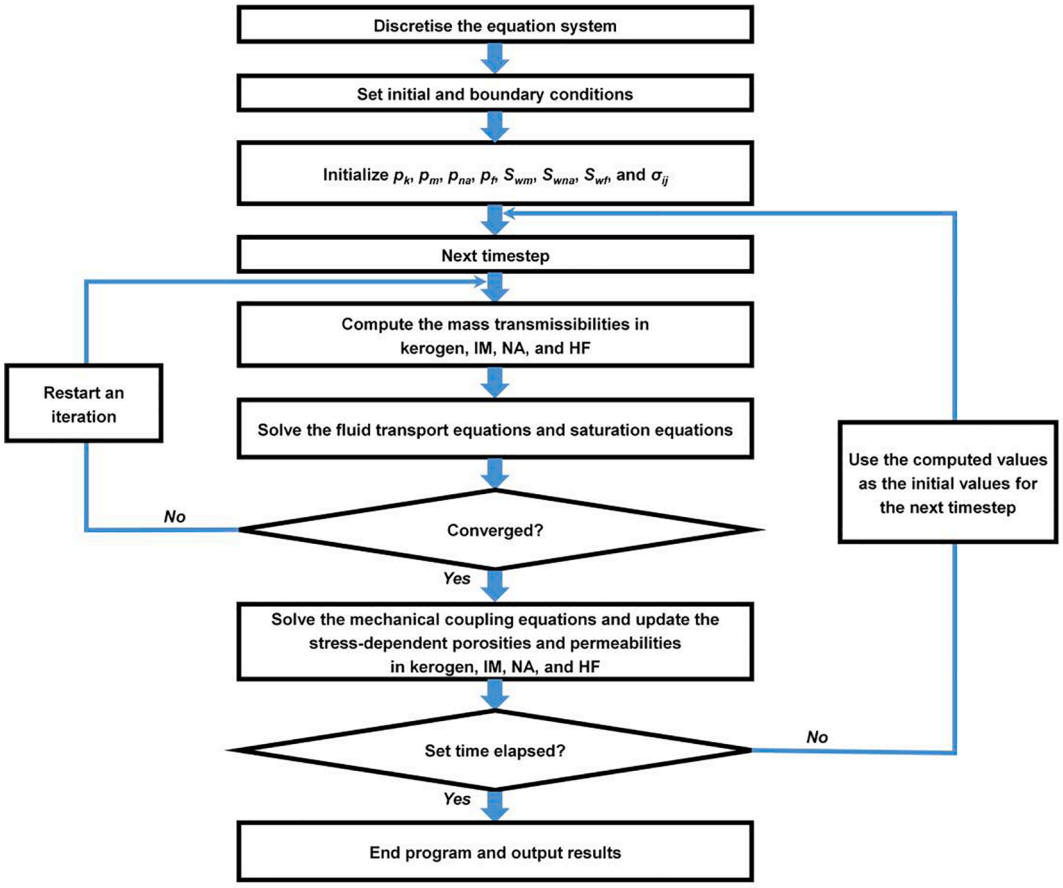

Fig. 8. Flow chart of the simulator.

$$\Delta G = \Delta G^*_{surf} \tag{28}$$

Combining Eqs., and, the term ΔG^* can be cancelled out, giving the following equation linking the wettability parameters, stress-dependent kerogen porosity, and $(p_k - p_m)$:

$$p_k - p_m = \gamma_{g-w}\theta^2_{eff}\sqrt{\frac{8\pi}{27A^*(1-\cos\theta_{eff})(1-\phi_{k,stress})}} \tag{29}$$

Obviously, if the quasi-equilibrium state shown in Fig. 4 also denotes the critical state in which the gas in kerogen with water film is about to be liberated. The term $(p_k - p_m)$ in this critical state just corresponds to the threshold differential pressure (*KTP*). Thus, we obtain the final expression of *KTP*:

$$KTP = \gamma_{g-w}\theta^2_{effc}\sqrt{\frac{8\pi}{27A^*_c(1-\cos\theta_{effc})(1-\phi_{k,stress})}} \tag{30}$$

where A^*_c is a characteristic contact area, while θ_{effc} is a characteristic contact angle. They denote the spherical cap area and the effective contact angle in the critical state of gas liberation, respectively. For a certain shale material, a known gas, and the water with a known salinity, these two parameters can be obtained by combining the microscopic imaging techniques and the captive-bubble method [52,53].

It should also be noted that $\gamma_{g\text{-}w}$ changes with T and p_k. Many previous publications provide the relevant data determined in laboratory by using the instruments such as modified interfacial tensiometer based on the pendent drop method [54,55]. For example, when the reservoir temperature is 353.15 K, the varying values of $\gamma_{g\text{-}w}$ with p_k are tested by Ren et al. [55] are plotted in Fig. 6:

The new *KTP* model presented in Eq. suggests that whether the gas can be released from the kerogen with water film depends on the combined effects of the pore pressure difference between kerogen and IM, fluid wettability at the kerogen surface, and stress-dependent porosity. By using this model, the control function *switch*(p_k, p_m) can be figured out, and the on/off mechanism for gas liberation can be expressed. Combining Eqs., and, we obtain the full form of the governing equation of gas transport in kerogen:

$$\begin{cases} \dfrac{\partial(\rho_{gk}\phi_{k,stress}+\rho_a\rho_s V_{ads})}{\partial t} + \nabla\cdot\left(-\rho_{gk}\dfrac{k_{kapp}}{\mu_g}\nabla p_k\right) = -Q_{k-m} \\ Q_{k-m} = \dfrac{D_{k-m}\rho_{gk}k_{k,stress}}{\mu_g}(p_k-p_m)\left[S_{gm}+S_{wm}\cdot switch(p_k,p_m)\right] \\ \phi_{k,stress} = \phi_{k0}\exp\{-C_k[(\overline{\sigma}-\overline{\sigma_0})-\alpha_k(p_k-p_{k0})]\} \\ k_{k,stress} = k_{k0}\exp\{-3C_k[(\overline{\sigma}-\overline{\sigma_0})-\alpha_k(p_k-p_{k0})]\}\cdot\dfrac{f_k(Kn_k)}{f_k(Kn_{k0})} \\ V_{ads} = \dfrac{V_L p_k}{P_L+p_k} \\ switch(p_k,p_m) = \begin{cases} 1.\ if\ p_k-p_m > KTP \\ 0, if\ p_k-p_m \le KTP \end{cases} \\ KTP = \gamma_{g-w}\theta^2_{effc}\sqrt{\dfrac{8\pi}{27A^*_c(1-\cos\theta_{effc})(1-\phi_{k,stress})}} \end{cases} \tag{31}$$

3.3. Gas-water-two-phase flow in inorganic matrix

3.3.1. Governing equation of IM

In IM, the adsorbed gas storage is ignored, and the gas–water-two-phase flow is considered because of the hydrophilic characteristic of IM

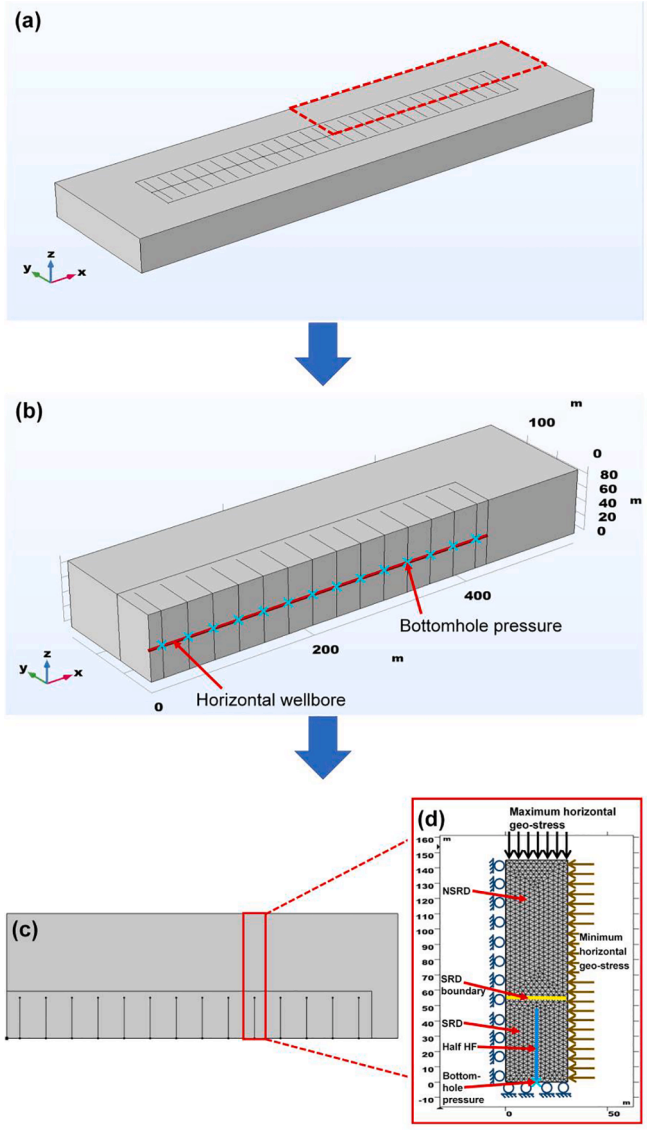

Fig. 9. Geometry simplification and boundary condition of the simulation case for Barnett Shale. (a) 3D geometry of the whole reservoir. (b) 3D geometry of a quarter of the reservoir. (c) Top view of a quarter of the reservoir; (d) A half hydraulic fracking segment including a half-length HF, SRD, and NSRD. The cyan "×" symbols represent the bottom-hole pressure points at which the gas flows into the wellbore. (For interpretation of the references to colour in this figure legend, the reader is referred to the web version of this article.)

pores. These inorganic pores have little adsorption amount, and spontaneously hold water by capillary imbibition. Based on the two-phase Darcy's law [14,16,36,56], the governing equation for water and gas transport in IM can be written as:

$$\begin{cases} \dfrac{\partial(\rho_{gm}\phi_{m,stress}S_{gm})}{\partial t} + \nabla\cdot\left(-\rho_{gm}\dfrac{k_{mapp}k_{rgm}}{\mu_g}\nabla p_{gm}\right) = Q_{k-m} - Q_{g,m-na} \\ \dfrac{\partial(\rho_w\phi_{m,stress}S_{wm})}{\partial t} + \nabla\cdot\left[-\rho_w\dfrac{k_{m,stress}k_{rwm}}{\mu_w}\nabla p_{wm}\right] = -Q_{w,m-na} \end{cases} \tag{32}$$

where the first equation is for the gas flow in IM, and the second equation is for the water flow in IM. ρ_{gm} is the gas density in IM, computed according to p_{gm} and the real gas equation of state (see **Appendix 3A**); k_{mapp} is the apparent gas permeability in IM; $\phi_{m,stress}$ is the stress-dependent IM porosity; $k_{m,stress}$ is the stress-dependent IM permeability; $Q_{k\text{-}m}$ is the mass source term of kerogen supplying gas to IM; $-Q_{g,m\text{-}na}$ is the mass sink term of IM supplying gas to NA; $-Q_{w,m\text{-}na}$ is the mass sink term of IM supplying water to NA; ρ_w is the water density; k_{rgm} is the relative permeability of gas in IM; k_{rwm} is the relative permeability of water in IM; μ_w is the water viscosity.

3.3.2. Porosity and permeability models

Similar to those of kerogen, the stress-dependent porosity of IM can be determined by applying Cui-Bustin's model:

$$\phi_{m,stress} = \phi_{m0}\exp\{-C_m[(\overline{\sigma}-\overline{\sigma_0}) - \alpha_m(p_m - p_{m0})]\} \tag{33}$$

where ϕ_{m0} is the initial IM porosity; C_m is the pore compressibility of IM, defined as $C_m = \alpha_m/(\phi_{m0}K_m)$ [4,40,41]; p_{m0} is the initial pore pressure in IM. It should be noted that the IM pore pressure (p_m) here is the average fluid pressure given by Eq.. The evolution of p_m influences the effective stress of IM $[(\overline{\sigma}-\overline{\sigma_0}) - \alpha_m(p_m - p_{m0})]$.

Furthermore, considering the effect of gas flow regime, the apparent gas permeability in IM can be expressed as:

$$k_{mapp} = k_{m,stress}\frac{f(Kn_m)}{f(Kn_{m0})} \tag{34}$$

where Kn_m is the Knudsen number in IM; Kn_{m0} is the initial Knudsen number in IM. They can be calculated according to the method given in **Appendix 3B**. $k_{m,stress}$ is the stress-dependent permeability of IM based on Cui-Bustin's model:

$$k_{m,stress} = k_{m0}\exp\{-3C_m[(\overline{\sigma}-\overline{\sigma_0}) - \alpha_m(p_m - p_{m0})]\} \tag{35}$$

where k_{m0} is the initial absolute permeability of IM.

3.3.3. Mass source-sink term

The gas sink term ($-Q_{g,m\text{-}na}$) and the water sink term ($Q_{w,m\text{-}na}$) of IM supplying fluids to NA are defined based on the theory proposed by Kazemi et al. [43]:

$$Q_{g,m-na} = \frac{D_{m-na}\rho_{gm}k_{mapp}k_{rgm}}{\mu_g}(p_{gm} - p_{gna}) \tag{36}$$

$$Q_{w,m-na} = \frac{D_{m-na}\rho_w k_{m,stress}k_{rwm}}{\mu_w}(p_{wm} - p_{wna}) \tag{37}$$

where $D_{m\text{-}na}$ is a shape factor related to the mean IM block size. For cubic IM blocks separated by the natural fractures, $D_{k\text{-}m} = 8/L_m^2$, where L_m is the mean length of the IM blocks (i.e., the mean natural fractures spacing).

3.3.4. Saturation equation and capillary pressure

As an additional constraint, the gas and water saturations in IM should obey the following relation:

$$S_{gm} + S_{wm} = 1 \tag{38}$$

The difference between gas pressure and water pressure in IM is defined as IM capillary pressure (p_{cm}):

$$p_{gm} - p_{wm} = p_{cm} \tag{39}$$

p_{cm} is a function of S_{wm}. For a given S_{wm}, the p_{cm}, gas relative permeability (k_{rgm}), water relative permeability (k_{rwm}), and gas relative permeability (k_{rwm}) can be directly calculated by using the analytical model proposed by Brooks and Corey [57], as detailed in **Appendix 3C**. Combining Eqs., and, we obtain the full form of the governing equation of fluid transport in IM:

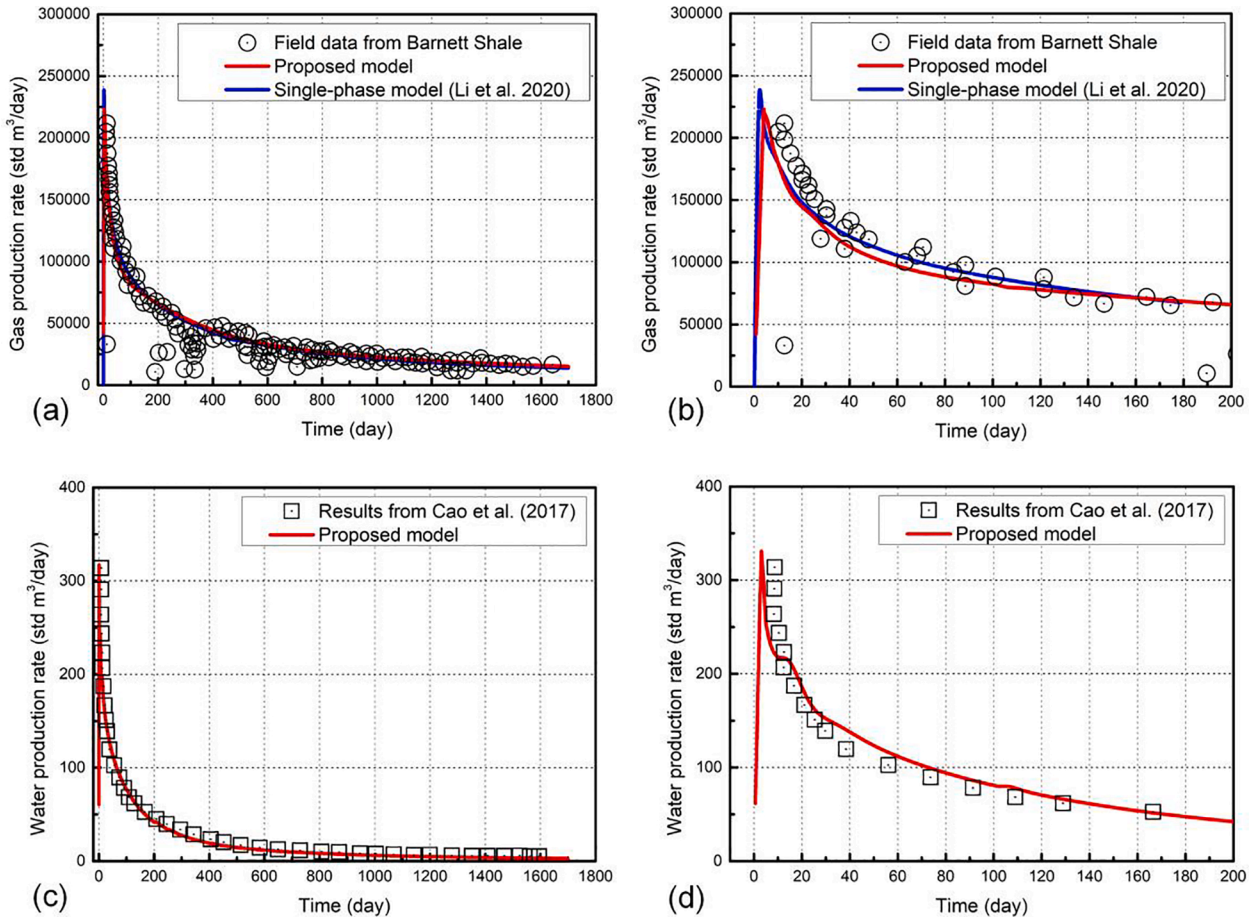

Fig. 10. Production history match for Barnett Shale. (a) Daily gas production: The scattered dots denote the field data; the red line denotes the simulation results computed by using the model proposed in this work; the blue line denotes the results computed by using the single-phase model proposed by Li et al. [4]. (b) Detailed daily gas production in the first 200 days. (c) Daily water production: The scattered squares denote the results numerically computed by Cao et al. [14]; the red line denotes the results computed by using the model proposed in this work. (d) Detailed daily water production in the first 200 days. (For interpretation of the references to colour in this figure legend, the reader is referred to the web version of this article.)

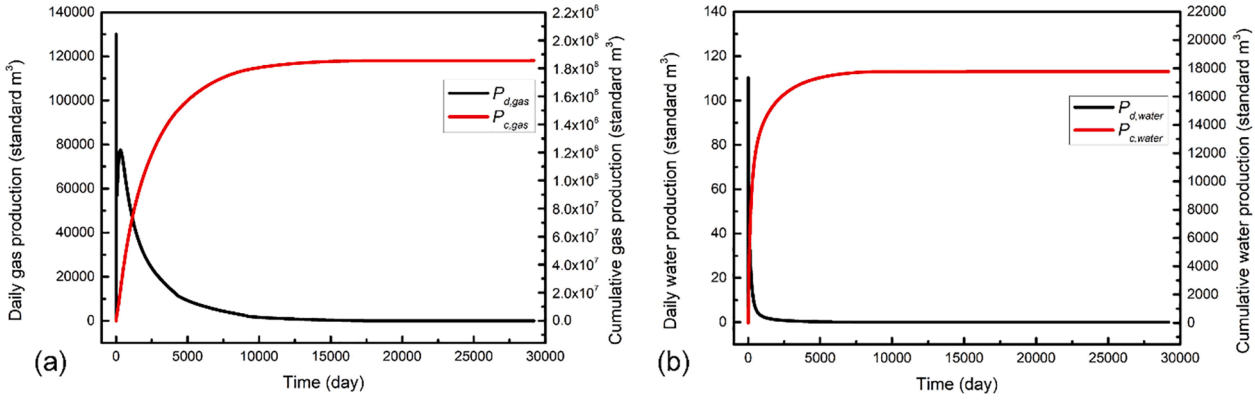

Fig. 11. Production curves of the base case during 29200-day gas extraction process. (a) Daily and cumulative gas production curves. (b) Daily and cumulative water production curves.

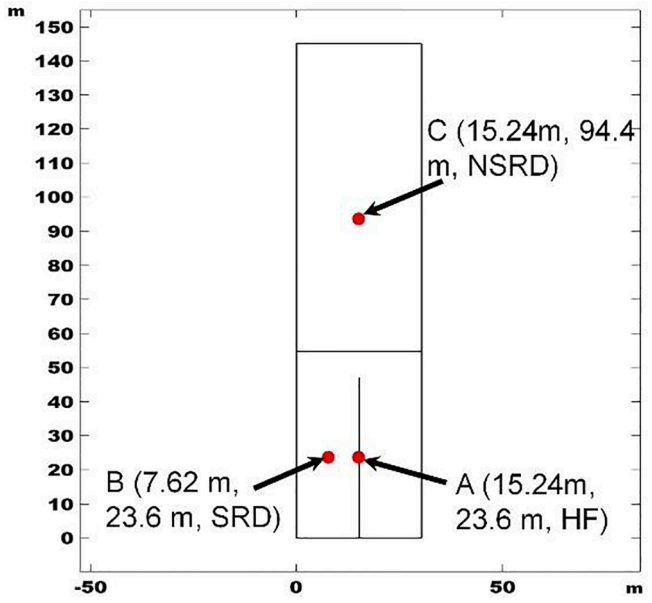

Fig. 12. Inspection points representing different domains in the geometry of the base case: Point A – HF; Point B – SRD; and Point C – NSRD.

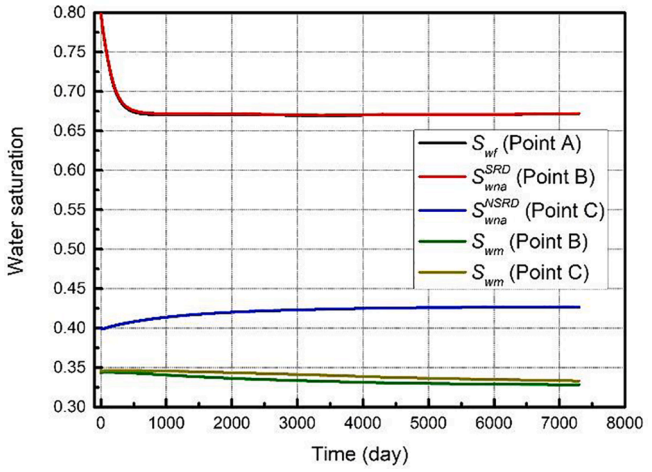

Fig. 13. Evolutions of water saturations of HF, NA, and IM in different locations.

$$\begin{cases} \dfrac{\partial(\rho_{gm}\phi_{m,stress}S_{gm})}{\partial t} + \nabla\cdot\left(-\rho_{gm}\dfrac{k_{mapp}k_{rgm}}{\mu_g}\nabla p_{gm}\right) = Q_{k-m} - Q_{g,m-na} \\ \dfrac{\partial(\rho_w\phi_{m,stress}S_{wm})}{\partial t} + \nabla\cdot\left[-\rho_w\dfrac{k_{m,stress}k_{rwm}}{\mu_w}\nabla p_{wm}\right] = -Q_{w,m-na} \\ \phi_{m,stress} = \phi_{m0}\exp\{-C_m[(\bar{\sigma}-\bar{\sigma}_0) - \alpha_m(p_m - p_{m0})]\} \\ k_{mapp} = k_{m0}\exp\{-3C_m[(\bar{\sigma}-\bar{\sigma}_0) - \alpha_m(p_m - p_{m0})]\}\cdot\dfrac{f(Kn_m)}{f(Kn_{m0})} \\ Q_{g,m-na} = \dfrac{D_{m-na}\rho_{gm}k_{mapp}k_{rgm}}{\mu_g}(p_{gm} - p_{gna}) \\ Q_{w,m-na} = \dfrac{D_{m-na}\rho_w k_{m,stress}k_{rwm}}{\mu_w}(p_{wm} - p_{wna}) \\ S_{gm} + S_{wm} = 1 \\ p_{gm} - p_{wm} = p_{cm} \end{cases} \tag{40}$$

3.4. Gas-water-two-phase flow in natural fractures network

3.4.1. Governing equation of NA

The natural fractures network (NA) in the proposed model refers to an inorganic continuum with relatively higher initial porosity, initial absolute permeability, initial water saturation, and lower bulk modulus compared to those of IM. Moreover, these NA properties are differently set in SRD and NSRD domains to reflect the multidomain effect caused by hydraulic fracking. The effects of gas flow regime on gas apparent permeability and gas sorption are ignored in NA [26]. With a similar form with Eq., the governing equation for gas–water-two-phase flow in NA can be written as:

$$\begin{cases} \dfrac{\partial\left(\rho^j_{gna}\phi^j_{na,stress}S^j_{gna}\right)}{\partial t} + \nabla\cdot\left(-\rho^j_{gna}\dfrac{k^j_{na,stress}k^j_{rgna}}{\mu_g}\nabla p^j_{gna}\right) = Q_{g,m-na} \\ \dfrac{\partial\left(\rho_w\phi^j_{na,stress}S^j_{wna}\right)}{\partial t} + \nabla\cdot\left(-\rho_w\dfrac{k^j_{na,stress}k^j_{rwna}}{\mu_w}\nabla p^j_{wna}\right) = Q_{w,m-na} \end{cases} \tag{41}$$

where the superscript j is the domain indicator, $j = SRD$ or $NSRD$; ρ_{gna} is the gas density in NA, computed according to p_{gna} and the real gas equation of state (see **Appendix 3A**);$\phi_{na,stress}$ is the stress-dependent NA porosity; $k_{na,stress}$ is the stress-dependent NA permeability; $Q_{g,m\text{-}na}$ is the source term of IM supplying gas to NA; $Q_{w,m\text{-}na}$ is the source term of IM supplying water to NA; k_{rgna} is the relative permeability of gas in NA; k_{rwna} is the relative permeability of water in NA.

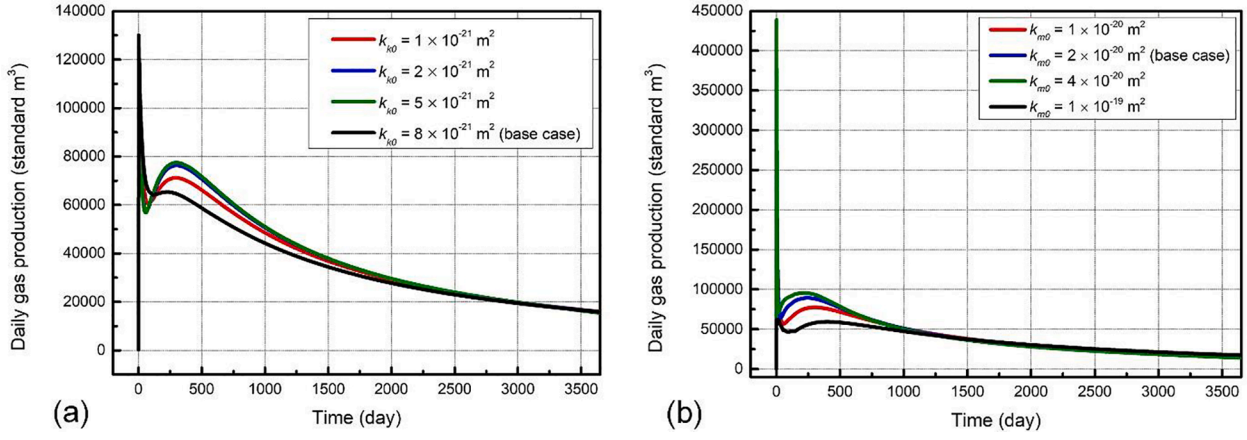

Fig. 14. Effects of initial absolute (apparent) permeabilities of kerogen and IM on daily gas production (0–3650 day). (a) Daily gas production curves with different k_{k0}s. (b) Daily gas production curves with different k_{m0}s.

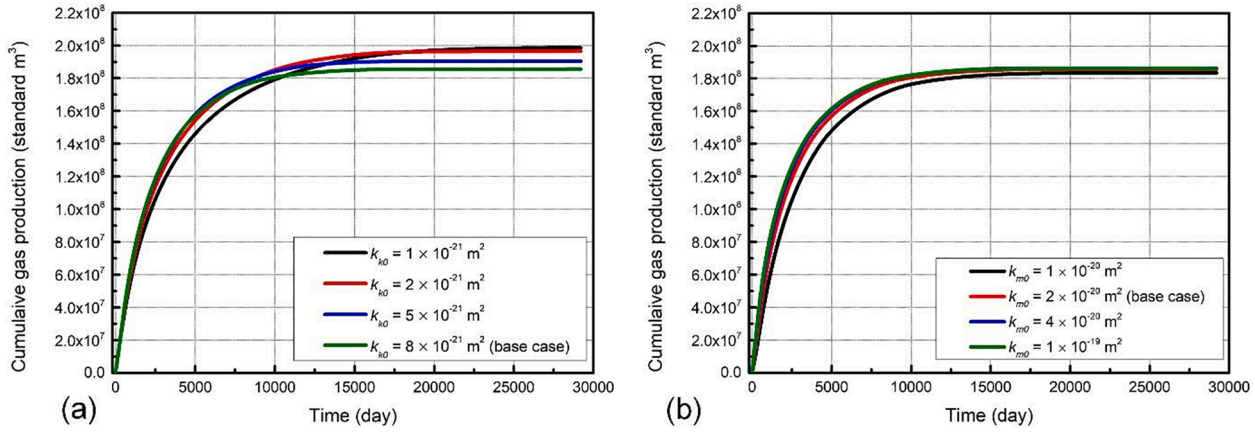

Fig. 15. Effects of initial absolute permeabilities of kerogen and IM on cumulative gas production. (a) Cumulative gas production curves with different k_{k0}s. (b) Cumulative gas production curves with different k_{m0}s.

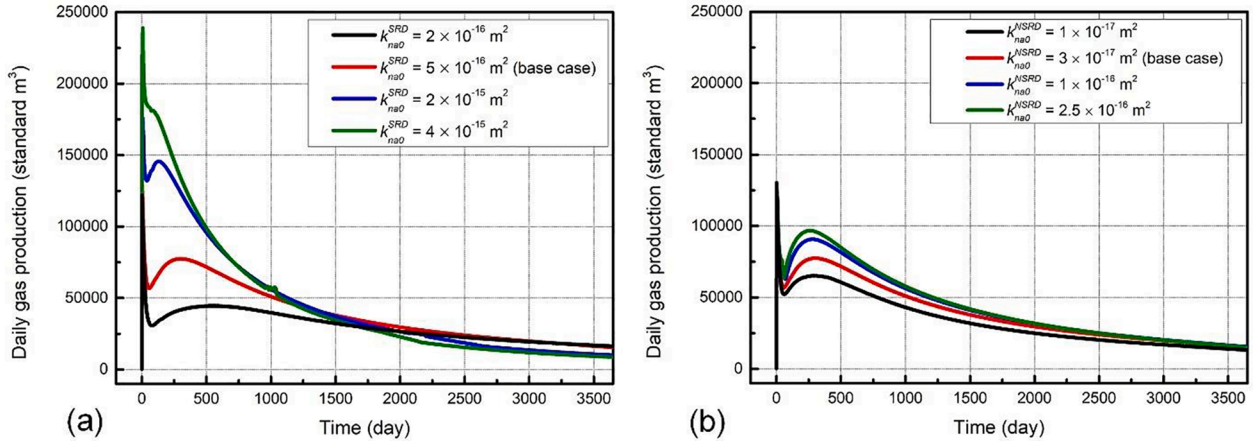

Fig. 16. Effects of initial absolute permeabilities of NA-SRD and NA-NSRD on daily gas production (0–3650 day). (a) Daily gas production curves with different k_{na0}^{SRD} s. (b) Daily gas production curves with different k_{na0}^{NSRD} s.

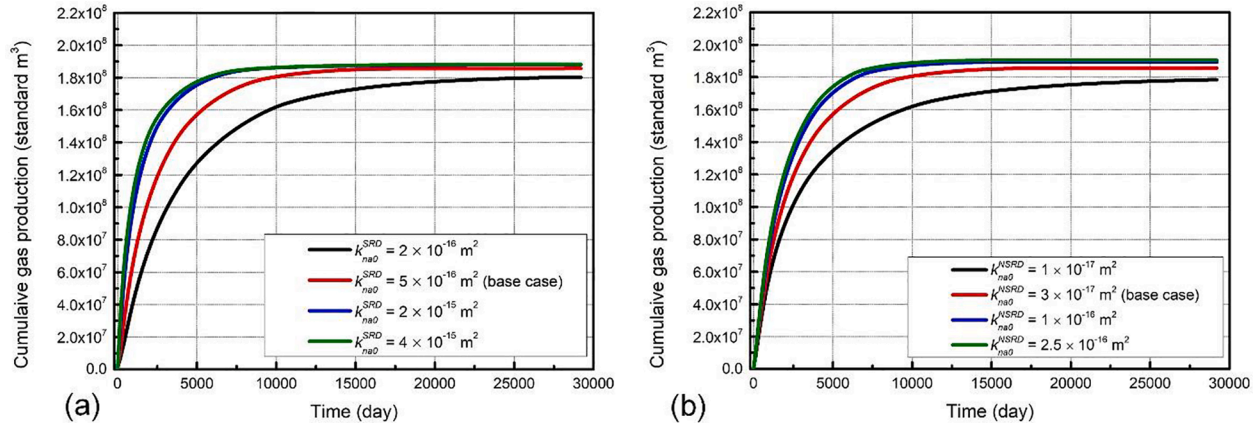

Fig. 17. Effects of initial absolute permeabilities of NA-SRD and NA-NSRD on cumulative gas production. (a) Cumulative gas production curves with different k_{na0}^{SRD} s. (b) Cumulative gas production curves with different k_{na0}^{NSRD} s.

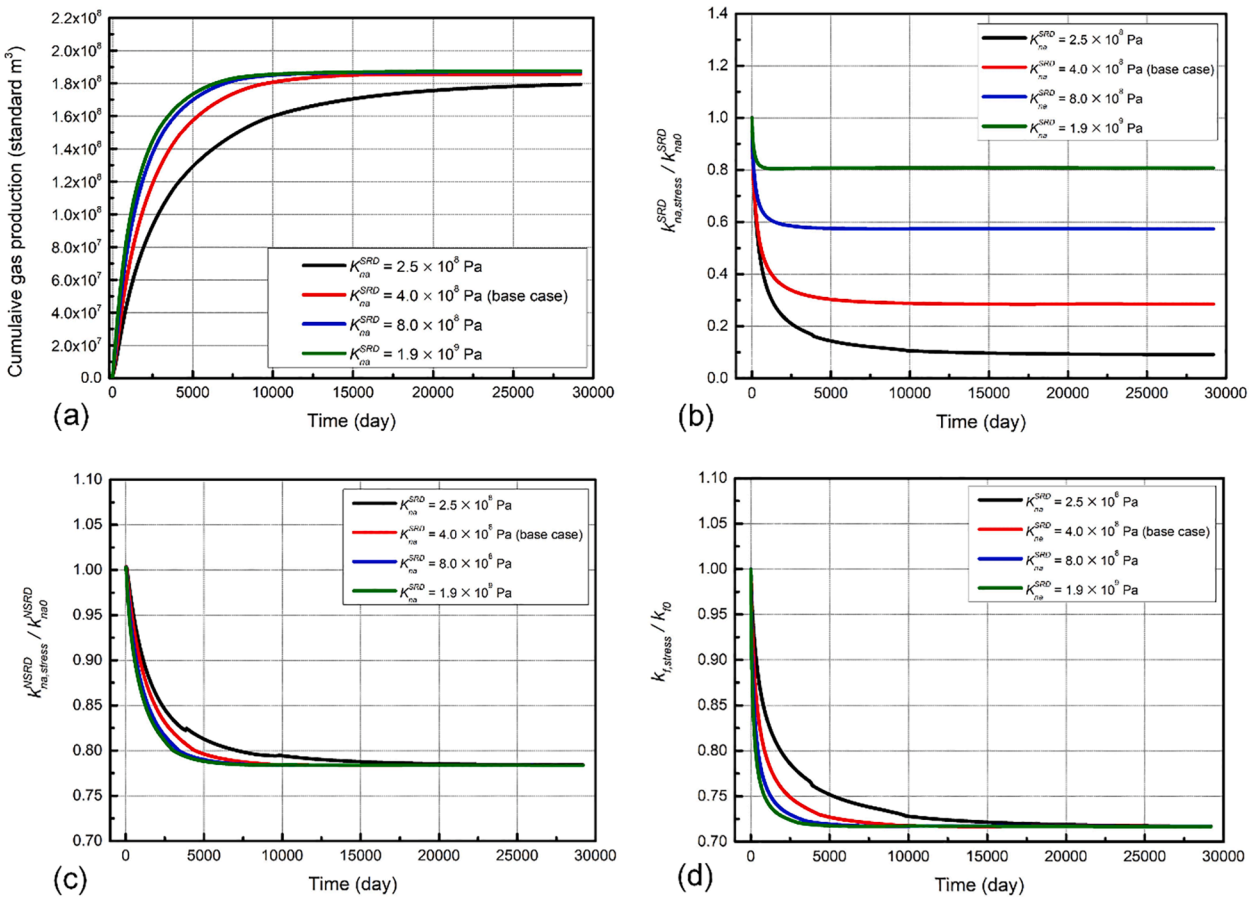

Fig. 18. Effects of NA-SRD bulk modulus on the gas extraction process. (a) Effect on cumulative gas production. (b) Effect on stress-dependent permeability of NA-SRD. (c) Effect on stress-dependent permeability of NA-NSRD. (d) Effect on stress-dependent permeability of HF.

3.4.2. Porosity and permeability models

Applying Cui-Bustin's model again, the stress-dependent porosity and permeability of NA can be expressed as:

$$\phi_{na,stress}^{j} = \phi_{na0}^{j}\exp\{-C_{na}^{j}\left[(\overline{\sigma}-\overline{\sigma_0})-\alpha_{na}^{j}\left(p_{na}^{j}-p_{na0}\right)\right]\} \tag{42}$$

$$k_{na,stress}^{j} = k_{na0}^{j}\exp\{-3C_{na}^{j}\left[(\overline{\sigma}-\overline{\sigma_0})-\alpha_{na}^{j}\left(p_{na}^{j}-p_{na0}\right)\right]\} \tag{43}$$

where ϕ_{na0} is the initial NA porosity; C_{na} is the pore compressibility of NA, defined as $C_{na} = \alpha_{na}/(\phi_{na0}K_{na})$; p_{na} is the pore pressure in NA given by Eq.; p_{na0} is the initial pore pressure in NA; k_{na0} is the initial absolute permeability of NA.

3.4.3. Saturation equation and capillary pressure

Similar to those in IM, the gas and water saturations in NA should obey the following relation:

$$S_{gna} + S_{wna} = 1 \tag{44}$$

The difference between gas pressure and water pressure in NA is defined as NA capillary pressure (p_{cna}):

$$p_{gna} - p_{wna} = p_{cna} \tag{45}$$

p_{cna}, k_{rgna}, and k_{rwna} are calculated by using the model proposed by Brooks and Corey [57], as detailed in **Appendix 3C**.

3.4.4. Continuity at boundaries

It should be emphasized that the continuities of the pore pressure, mass flow rate of gas (q_{gna}^{j}), mass flow rate of water (q_{wna}^{j}), gas saturation, and water saturation in NA at the boundary between SRD and NSRD should be ensured:

$$\begin{cases} p_{na}^{NSRD}|at\ SRD\ boundary = p_{na}^{SRD}|at\ SRD\ boundary; \\ q_{gna}^{NSRD}|at\ SRD\ boundary = q_{gna}^{SRD}|at\ SRD\ boundary; \\ q_{wna}^{NSRD}|at\ SRD\ boundary = q_{wna}^{SRD}|at\ SRD\ boundary; \\ S_{gna}^{NSRD}|at\ SRD\ boundary = S_{gna}^{SRD}at\ SRD\ boundary; \\ S_{wna}^{NSRD}|at\ SRD\ boundary = S_{wna}^{SRD}|at\ SRD\ boundary \end{cases} \tag{46}$$

Meanwhile, the continuities of the pore pressure, gas flow rate, water flow rate, gas saturation, and water saturation should also be satisfied at HF which can be considered as an outlet boundary of NA-SRD:

$$\begin{cases} p_{na}^{SRD}|at\ HF = p_{f}|at\ HF; \\ q_{gna}^{SRD}|at\ HF = q_{gf}|at\ HF\, q_{wna}^{SRD}|at\ HF = q_{wf}|at\ HF; \\ S_{gna}^{SRD}|at\ HF = S_{gf}|at\ HF\ \ S_{wna}^{SRD}|at\ HF = S_{wf}|at\ HF \end{cases} \tag{47}$$

where p_f is the pore pressure in HF, defined by Eq.; q_{gf} is the inlet mass flow rate of gas in HF; q_{wf} is the inlet mass flow rate of water in HF; S_{gf} is the gas saturation in HF; S_{wf} is the water saturation in HF. Combining Eqs., and, we obtain the full form of the governing equation of fluid transport in NA:

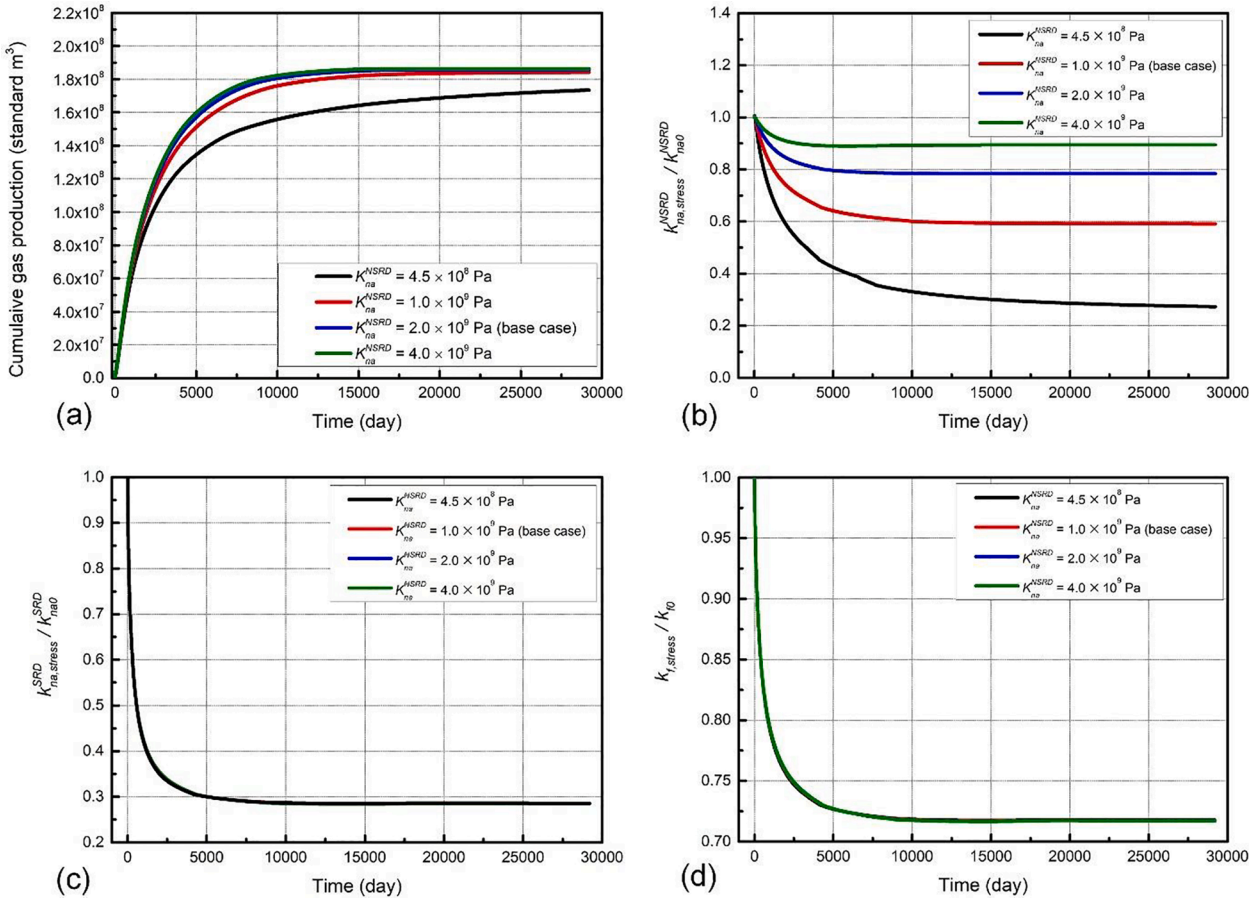

Fig. 19. Effects of NA-NSRD bulk modulus on the gas extraction process. (a) Effect on cumulative gas production. (b) Effect on stress-dependent permeability of NA-NSRD. (c) Effect on stress-dependent permeability of NA-SRD. (d) Effect on stress-dependent permeability of HF.

$$
\begin{cases}
\dfrac{\partial\left(\rho^j_{gna}\phi^j_{na,stress}S^j_{gna}\right)}{\partial t}+\nabla\cdot\left(-\rho^j_{gna}\dfrac{k^j_{na,stress}k^j_{rgna}}{\mu_g}\nabla p^j_{gna}\right)=Q_{g,m-na}\\
\dfrac{\partial\left(\rho_w\phi^j_{na,stress}S^j_{wna}\right)}{\partial t}+\nabla\cdot\left(-\rho_w\dfrac{k^j_{na,stress}k^j_{rwna}}{\mu_w}\nabla p^j_{wna}\right)=Q_{w,m-na}\\
\phi^j_{na,stress}=\phi^j_{na0}\exp\{-C^j_{na}\left[(\overline{\sigma}-\overline{\sigma_0})-\alpha^j_{na}\left(p^j_{na}-p_{na0}\right)\right]\}\\
k^j_{na,stress}=k^j_{na0}\exp\{-3C^j_{na}\left[(\overline{\sigma}-\overline{\sigma_0})-\alpha^j_{na}\left(p^j_{na}-p_{na0}\right)\right]\}\\
S_{gna}+S_{wna}=1\\
p_{gna}-p_{wna}=p_{cna}\\
p^{NSRD}_{na}|at\ SRD\ boundary\ =\ p^{SRD}_{na}|at\ SRD\ boundary;;\\
q^{NSRD}_{gna}|at\ SRD\ boundary=q^{SRD}_{gna}|at\ SRD\ boundary;\ q^{NSRD}_{wna}|at\ SRD\ boundary=q^{SRD}_{wna}|at\ SRD\ boundary;\\
S^{NSRD}_{gna}|at\ SRD\ boundary=S^{SRD}_{gna}|at\ SRD\ boundary;\ S^{NSRD}_{wna}|at\ SRD\ boundary=S^{SRD}_{wna}|at\ SRD\ boundary;\\
p^{SRD}_{na}|at\ HF\ =\ p_f|at\ HF;\\
q^{SRD}_{gna}|at\ HF=q_{gf}|at\ HF;q^{SRD}_{wna}|at\ HF=q_{wf}|at\ HF;\\
S^{SRD}_{gna}|at\ HF=S_{gf}|at\ HF;\ S^{SRD}_{wna}|at\ HF=S_{wf}|at\ HF
\end{cases}
\tag{48}
$$

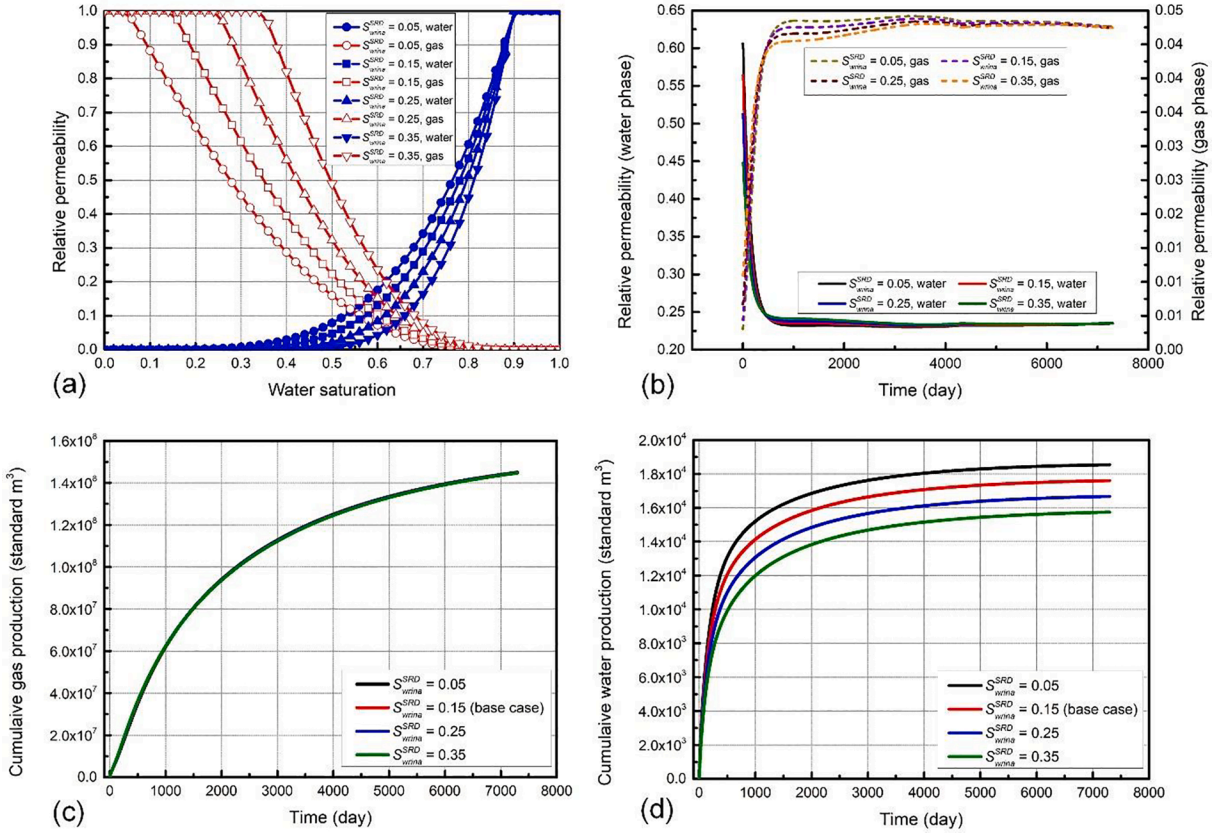

Fig. 20. Effects of irreducible water saturation of NA-SRD on gas/water production. (a) Relative permeability curves with different S_{wrina}^{SRD} s, calculated based on Brooks and Corey's model. (b) Relative permeabilities of NA at Point B of the base case during 7300-day production with different S_{wrina}^{SRD} s. (c) Cumulative gas productions with different S_{wrina}^{SRD} s. (d) Cumulative water productions with different S_{wrina}^{SRD} s.

3.5. Gas-water-two-phase flow in primary hydraulic fracture

3.5.1. Governing equation of HF

Primary hydraulic fracture (HF) is simplified as a 1D fractured medium. Meanwhile, it is also the outlet flow boundary of NA in SRD. HF bridges the horizontal wellbore and the bulk shale. Based on our previous study [4], the governing equation of gas–water-two-phase flow in HF can be given as the following form:

$$\begin{cases} \dfrac{\partial(\rho_{gf}\phi_{f,stress}S_{gf})}{\partial t} + \nabla_T\cdot\left[-b_{f,stress}\rho_{gf}\dfrac{k_{f,stress}k_{rgf}}{\mu_g}\nabla p_{gf}\right] = 0 \\ \dfrac{\partial(\rho_w\phi_{f,stress}S_{wf})}{\partial t} + \nabla_T\cdot\left[-b_{f,stress}\rho_{wf}\dfrac{k_{f,stress}k_{rwf}}{\mu_w}\nabla p_{wf}\right] = 0 \end{cases} \tag{49}$$

where ∇_T denotes the gradient operator restricted to the tangential plane of HF; ρ_{gf} is the gas density in HF, computed according to p_{gf} and the real gas equation of state (see **Appendix 3A**); $\phi_{f,stress}$ is the stress-dependent HF porosity; $k_{f,stress}$ is the stress-dependent HF permeability; k_{rgf} is the relative permeability of gas in HF; k_{rwf} is the relative permeability of water in HF.

3.5.2. Porosity and permeability models

Stress-dependent porosity and permeability of HF ($\phi_{f,stress}$ and $k_{f,stress}$) are determined by using the model proposed by Li et al. [4]. In this model, the evolution of the mean stress at a certain point in HF is converted into the change of pore pressure according to Biot's theory in poroelasticity:

$$\phi_{f,stress} = \phi_{f0}\exp\left[C_f\left(p_f - p_{f0}\right)\right] \tag{50}$$

$$k_{f,stress} = k_{f0}\exp\left\{2C_f\left(p_f - p_{f0}\right)\right\} \tag{51}$$

where ϕ_{f0} is the initial HF porosity; C_f is the pore compressibility of HF, defined as $C_f = \alpha_f/(\phi_{f0}K_f)$; p_{f0} is the initial pore pressure in HF; k_{f0} is the initial absolute HF permeability.

Besides, the stress-dependent HF aperture ($b_{f,stress}$) has the following expression:

$$b_{f,stress} = b_{f0}\exp\left[C_f\left(p_f - p_{f0}\right)\right] \tag{52}$$

where b_{f0} is the initial HF aperture.

3.5.3. Saturation equation and capillary pressure

Similar to IM and NA, the gas and water saturations in HF obey the following relation:

$$S_{gf} + S_{wf} = 1 \tag{53}$$

The difference between gas pressure and water pressure in HF is defined as HF capillary pressure (p_{cf}):

$$p_{gf} - p_{wf} = p_{cf} \tag{54}$$

p_{cf}, k_{rgf}, and k_{rwf} are calculated by using the model proposed by Brooks and Corey [57], as detailed in **Appendix 3C**.

3.5.4. Continuity at boundaries

Note that the inflow of HF is exactly provided by the outflow from SRD [see the boundary condition in Eq.]. That is why there is no mass source term on the right hand of the first equation in Eq.. Another boundary condition is that, at the intersection line of HF and the wellbore, the value of p_f equals the bottom-hole pressure (BHP):

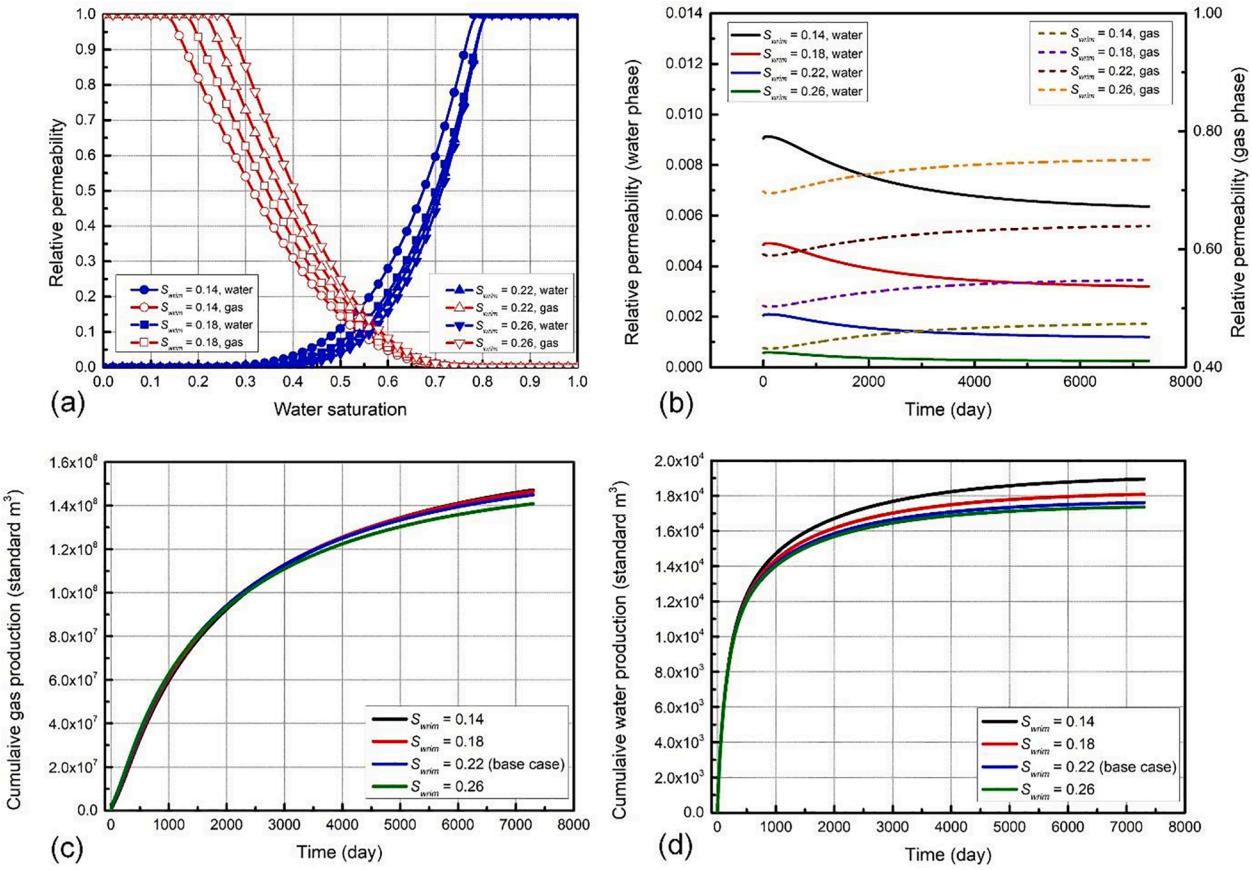

Fig. 21. Effects of irreducible water saturation of inorganic matrix on gas/water production. (a) Relative permeability curves with different S_{wrim}s, calculated based on Brooks and Corey's model. (b) IM relative permeabilities at Point B of the base case during 7300-day production with different S_{wrim}s. (c) Cumulative gas productions with different S_{wrim}s. (d) Cumulative water productions with different S_{wrim}s.

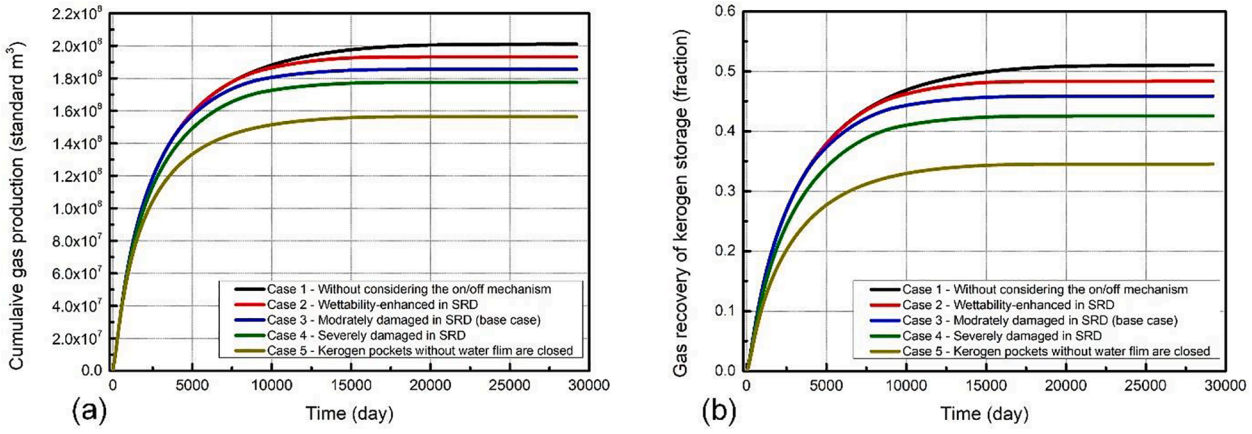

Fig. 22. Long-term gas production performances of the five cases with different wetting conditions in 29200-day extraction. (a) Cumulative productions; (b) Recovery of original gas in kerogen.

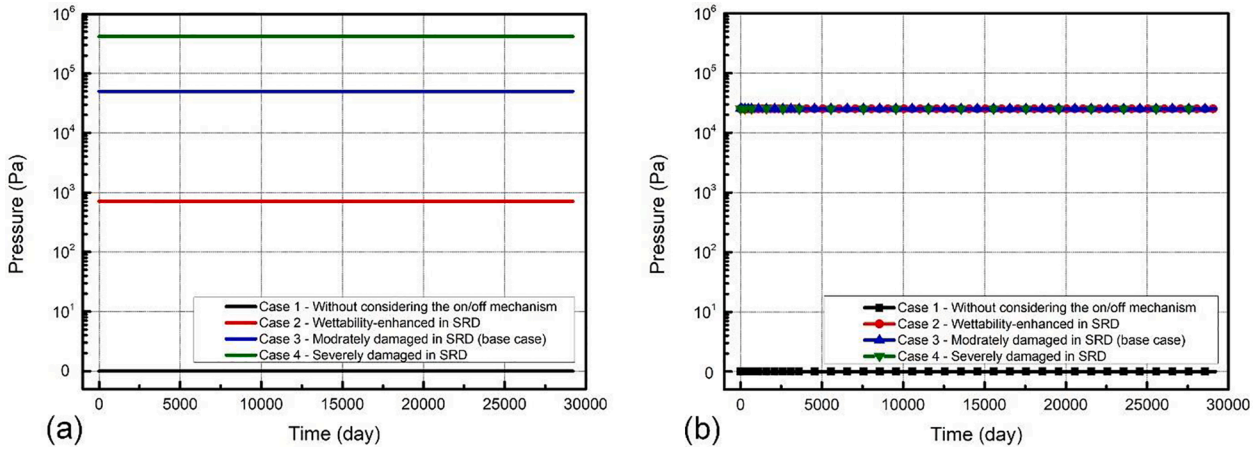

Fig. 23. *KTP*s in different domains for Cases 1 – 4 during 29200-day extraction. (a) *KTP*s in SRD (Point B); (b) *KTP*s in NSRD (Point C).

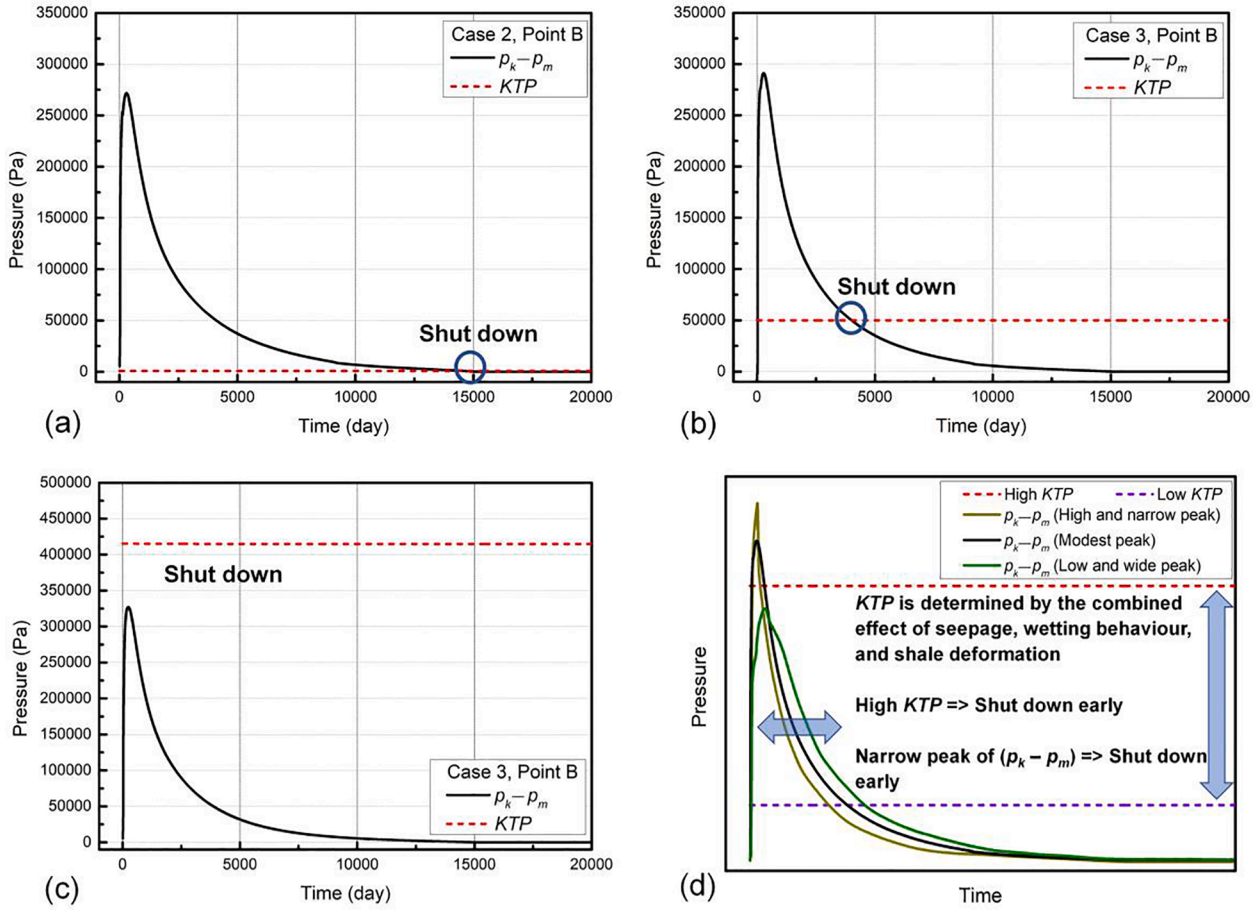

Fig. 24. Relationship between ($p_k - p_m$) and *KTP* curves for shale gas production. (a) ($p_k - p_m$) and *KTP* curves of Case 2; (b) ($p_k - p_m$) and *KTP* curves of Case 3; (c) ($p_k - p_m$) and *KTP* curves of Case 4; (d) Illustration of the key knowledge about the relationship between ($p_k - p_m$) and *KTP*.

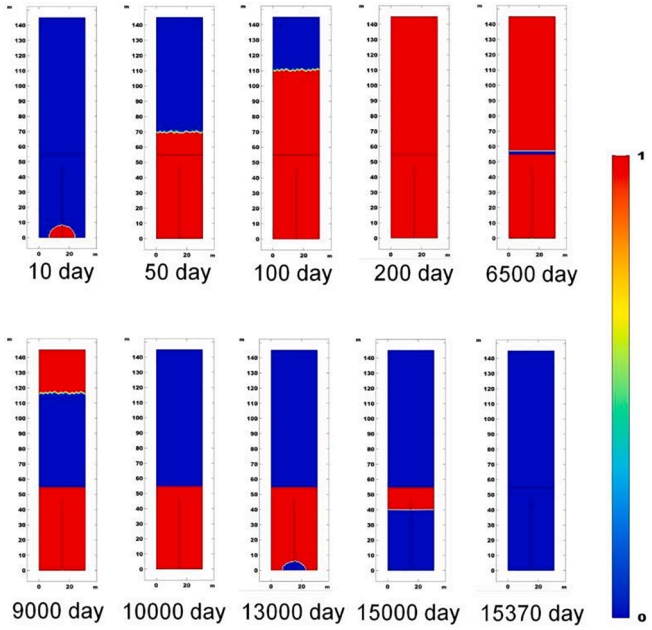

Fig. 25. Evolution of on/off state distribution of kerogen with water film for Cases 2 (SRD is wettability-enhanced). Red represents that the kerogen with water film is open [i.e., *switch*(p_k, p_m) = 1], while blue denotes that the kerogen with water film is closed [i.e., *switch*(p_k, p_m) = 0]. (For interpretation of the references to colour in this figure legend, the reader is referred to the web version of this article.)

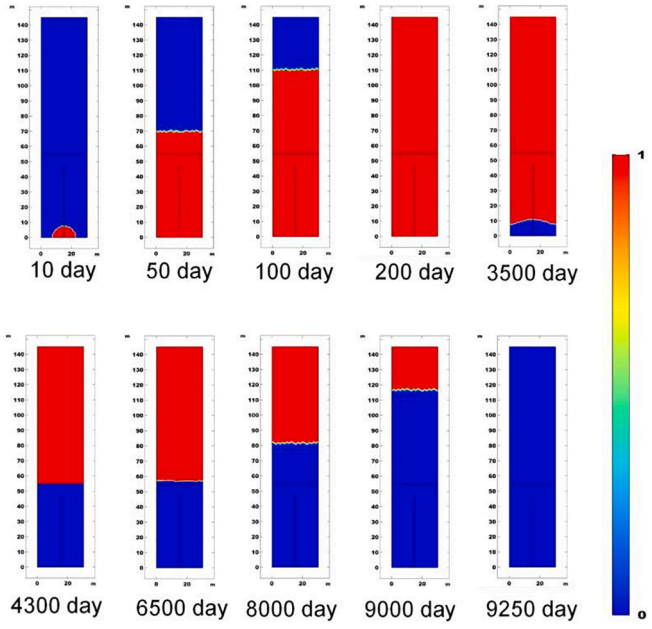

Fig. 26. Evolution of on/off state distribution of kerogen with water film for Cases 3 (SRD is moderately damaged). Red represents that the kerogen with water film is open [i.e., *switch*(p_k, p_m) = 1], while blue denotes that the kerogen with water film is closed [i.e., *switch*(p_k, p_m) = 0]. (For interpretation of the references to colour in this figure legend, the reader is referred to the web version of this article.)

$p_f|at\ wellbore = BHP$

Combining Eqs., and, we obtain the full form of the governing equation of HF:

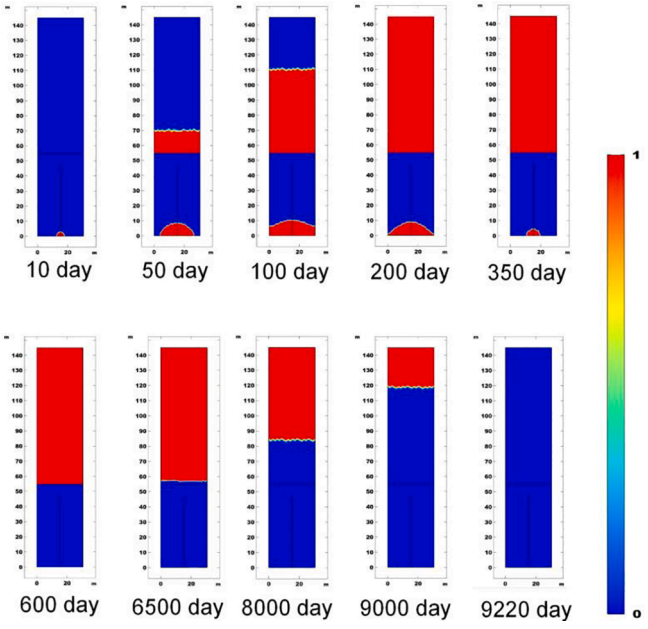

Fig. 27. Evolution of on/off state distribution of kerogen with water film for Cases 4 (SRD is severely damaged). Red represents that the kerogen with water film is open [i.e., *switch*(p_k, p_m) = 1], while blue denotes that the kerogen with water film is closed [i.e., *switch*(p_k, p_m) = 0].

$$\begin{cases} \dfrac{\partial(\rho_{gf}\phi_{f,stress}S_{gf})}{\partial t} + \nabla_T\cdot\left[-b_{f,stress}\rho_{gf}\dfrac{k_{f,stress}k_{rgf}}{\mu_g}\nabla p_{gf}\right] = 0 \\ \dfrac{\partial(\rho_w\phi_{f,stress}S_{wf})}{\partial t} + \nabla_T\cdot\left[-b_{f,stress}\rho_{wf}\dfrac{k_{f,stress}k_{rwf}}{\mu_w}\nabla p_{wf}\right] = 0 \\ \phi_{f,stress} = \phi_{f0}\exp\left[C_f\left(p_f - p_{f0}\right)\right] \\ k_{f,stress} = k_{f0}\exp\left\{2C_f\left(p_f - p_{f0}\right)\right\} \\ S_{gf} + S_{wf} = 1 \\ p_{gf} - p_{wf} = p_{cf} \\ p_{na}^{SRD}|at\ HF = p_f|at\ HF; \\ q_{gna}^{SRD}|at\ HF = q_{gf}|at\ HF; q_{wna}^{SRD}|at\ HF = q_{wf}|at\ HF; \\ S_{gna}^{SRD}|at\ HF = S_{gf}|at\ HF\ S_{wna}^{SRD}|at\ HF = S_{wf}|at\ HF \\ p_f|at\ wellbore = BHP \end{cases} \tag{56}$$

3.6. Coupling relationship of multiple physical processes

The partial differential equations Eqs., and construct the fully coupled, multidomain, and multiphysics model considering water effects for the evaluation of flowback from stimulated shale reservoirs. The relationship between different physics is summarized in Fig. 7. First of all, the mechanical coupling relationship [Eq.] globally controls the evolutions of stress-dependent porosity and permeability in different media and domains. In the second place, the complex flow processes in the various media [Eqs., and] are linked by the mass conservation law, resulting in different fluid phase distributions and pressure evolutions in these media. Thirdly, different properties in various domains caused by hydraulic fracking treatment can be conveniently input, which leads to distinct changes in these domains during shale gas extraction. Fourthly, by setting boundary conditions, the continuity of fluid flow is ensured. In brief, the complexities of multiple physical processes occurring in the stimulated shale gas reservoir are comprehensively incorporated in the proposed model.

3.7. Implementation of mathematical model

To implement the proposed mathematical model, we build a numerical simulator by using COMSOL Multiphysics (Version 5.5), a commercial PDE solver based on the finite element method (FEM), to fulfill the simulation of the production process of stimulated shale reservoirs. The flow chart of the simulator is shown in Fig. 8. Basically, a complete computation includes six parts [58]: (1) The simulator discretises the equation system to approximately convert the PDEs to linear equation groups; (2) According to the initial and boundary conditions, the simulator initializes the pressures and saturations in kerogen, IM, NA, and HF. The mean total stress is also initialized to obtain the initial stress-dependent porosities and permeabilities in kerogen, IM, NA, and HF; (3) At each timestep, the simulator computes the mass transmissibilities in kerogen, IM, NA, and HF according to the initialized pressures and saturations; (4) The simulator solves the discrete equation system including the fluid transport equations and saturation equations [Eqs.,] to update the primary variables (p_k, p_m, p_{na}, p_f, S_{wm}, S_{wna}, and S_{wf}). These computations are automatically performed by the multifrontal massively parallel sparse (MUMPS) direct solver in COMSOL Multiphysics; (5) If the computed residual converges, the simulator further solves the mechanical coupling equation [Eq.] by approximately converting the mechanical PDEs to linear equation groups to obtain a new displacement field. Then, the simulator converts the displacement into the strain/stress. Thus, a new distribution of the mean total stress can be calculated to further figure out the new stress-dependent porosities [by using Eqs., and] and permeabilities [by using Eqs., and] in kerogen, IM, NA, and HF for the next timestep. Otherwise, the simulator cycles back to re-compute the fluid transmissibilities until it converges at the current timestep. In the re-computation process, the simulator will adjust the initialization and/or decrease the length of the time step to try to satisfy the convergence criteria; (6) If the set time points for output are not all-done, the simulator moves to compute the new fluid transmissibilities for the next timestep with the updated variables. Otherwise, the computation terminates and the simulator outputs all the results of each timestep.

Here, we further briefly introduce the computation methods used by the commercial PDE solver. Variable-order variable-step-size backward differentiation formulas (BDF) are used to control the time-stepping process and solve the discretised time-dependent PDE problem [59,60]. The BDF solver using the backward Euler differentiation formulas has been widely used for many years and is known for its great stability and smoothing effect (the latter is particularly important for consistent initialization in the initial step of multiphysics coupling simulations). In each time step, the linearized equation groups are solved by the multifrontal massively parallel sparse (MUMPS) direct solver. It works on general systems of the form Ax = b and uses several preordering algorithms to permute the columns and thereby minimize the fill-in. Besides, the iterations are based on the Newton-Raphson method [61].

4. Model verification

To verify the multidomain and multiphysics model proposed in this work, a set of gas–water production data from a horizontal gas well in Barnett Shale with 28 hydraulic fracking segments in the United States is collected from the published literature [62,14] for data matching. The proposed model formulated in **Section 3** is implemented by using COMSOL Multiphysics (Version 5.5) so that the shale gas extraction process of the case can be numerically simulated. Here, the proposed model is applied in a 2D geometry (i.e., the thickness equals 1 m) to simulate a half hydraulic fracking segment as a representative part of the shale reservoir. The simplification from the 3D shale reservoir geometry to the 2D geometry is illustrated in Fig. 9. The 3D geometry of the whole Barnett reservoir is displayed in Fig. 9**(a)**. Due to the geometric symmetry, the 3D structure of a quarter of the reservoir framed by the red dashed line with the horizontal wellbore is further depicted in Fig. 9**(b)**. Note that the cyan "×" symbols represent the bottom-hole pressure points at which the gas flows into the wellbore. Furthermore, if the effect of gravity can be ignored, the 3D quarter of the reservoir can be simplified as a 2D geometry (i.e., the thickness equals 1 m) of which the top view is shown in Fig. 9**(c)**. In this geometry, the simulated gas flow process is 2D, while the simulated deformation process is related to the plain stress and strain. The 2D quarter of the reservoir includes 14 half hydraulic fracking segments. According to the geometric symmetry, the gas and water extraction process in a half hydraulic fracking segment [see Fig. 9 **(d)**] is first simulated to obtain the daily gas production ($P_{d,gas,2D}$) and daily water production ($P_{d,water,2D}$). After that, the total daily gas production ($P_{d,gas}$) and the total daily water production ($P_{d,water}$) of the whole (3D) reservoir can be simply figured out as follows:

$$P_{d,gas} = 4Nd_{res}P_{d,gas,2D} \tag{57}$$

$$P_{d,water} = 4Nd_{res}P_{d,water,2D} \tag{58}$$

where N is the number of half hydraulic fracking segments in a quarter of the reservoir. In this case, $N = 14$; d_{res} is the thickness of the reservoir. This simplification method has been successfully used to evaluate shale gas production by Cheng [11] and Liu et al. [15] so that the computation time can be much decreased with acceptable accuracy. It should also be noted that each half hydraulic fracking segment is under a geo-stress field orthogonally decomposed as the maximum horizontal geo-stress and the minimum horizontal geo-stress, while the roller constraints are set along the horizontal wellbore and the left boundary, as shown in Fig. 9 **(d)**. These settings reflect the influence of the in-situ-geo-stress field on shale deformation [4,23,24].

The reservoir properties and modelling parameters used for the simulation case of Barnett Shale are listed in Table 1. These parameters are extracted from the previously published studies [4,11,14,15,62] except those related to the wettability/interfacial properties for the calculation of *KTP* because *KTP* is a new concept proposed in this work. These wettability/interfacial properties include characteristic contact area (A_c^*), characteristic contact angle (θ_{effc}), and gas–water interfacial tension (γ_{g-w}). As a reflection of the difference between SRD and NSRD caused by hydraulic fracking treatment, the NA-SRD and NA-NSRD have different bulk moduli, entry pressure for two-phase flow, initial porosity, initial absolute permeability, and initial water saturation. Specifically, $K_{na}^{SRD} < K_{na}^{NSRD}$, $p_{ena}^{SRD} < p_{ena}^{NSRD}$, $\phi_{na0}^{SRD} > \phi_{na0}^{NSRD}$, and $k_{na0}^{SRD} > k_{na0}^{NSRD}$ are caused by the generation of secondary hydraulic fractures and the enhancement of the natural fractures in SRD, while $S_{wna0}^{SRD} > S_{wna0}^{NSRD}$ is originated from the invasion of water-based fracking fluids (such as slickwater) into SRD. More importantly, the wettability/interfacial properties in SRD (containing the mixture of the connate brine and the invaded fracking fluids) and NSRD (only containing the connate brine) are different. Specifically, $A_c^{*SRD} < A_c^{*NSRD}$, $\theta_{effc}^{SRD} > \theta_{effc}^{NSRD}$, and $\gamma_{g-w}^{SRD} = 1.1 \times \gamma_{g-w}^{SRD}$. These differences, reflecting the fact that the invasion of external fluids influences the gas liberation from kerogen in SRD, will be discussed in **Section 5.3**. The different settings of the parameters in various domains also indicate the great flexibility of our model in differentiating SRD and NSRD. According to the practical demand of simulation, more reservoir parameters may be set differently in SRD and NSRD to fully consider the difference between these two distinct domains in multiple aspects. These parameter differences can be obtained in advance by field logging, well-test analysis, or geological information techniques [4,7].

The data-matching results presented in Fig. 10**(a)** demonstrate that the daily gas production curve for 1700-day extraction simulated by using the proposed model is highly consistent with the field data. As a comparison, a multidomain numerical model based on a single (gas) phase flow proposed by Li et al. [4] is also used to match the same gas production data. To show more details about the early stage of the gas extraction process, the field data and simulation results of the two models during the first 200 days are particularly shown in Fig. 10**(b)**. It

Table 1
Reservoir properties and modelling parameters for the case of Barnett Shale. The parameters are collected from published studies [4,11,14,15,62].

Parameter	Value	Symbol	Unit
Simulation model dimension: length × width × thickness	30.48 × 145 × 90	–	m × m × m
Simulated SRD dimension: length × width × thickness	30.48 × 54.8 × 90	–	m × m × m
Half length of HF	47.2	–	m
Reservoir temperature	353.15	T	K
Number of HFs	28	N	–
Maximum horizontal geo-stress	41.6×10^6	–	Pa
Minimum horizontal geo-stress	37.3×10^6	–	Pa
Initial pore pressure of reservoir	20.34×10^6	p_{k0}, p_{m0}, p_{na0}, and p_{f0}	Pa
Bottom-hole pressure	3.69×10^6	BHP	Pa
Shale density	2460	ρ_s	kg/m^3
Molar weight of methane	0.016	M	kg/mol
Gas viscosity	1.84×10^{-5}	μ_g	Pa•s
Water density	971.8	μ_w	kg/m^3
Langmuir volume constant	0.00272	V_L	m^3/kg
Langmuir strain constant	0.008	ε_L	–
Volumetric fraction of kerogen	0.05	η_k	–
Bulk modulus of kerogen	5.0×10^9	K_k	Pa
Poisson's ratio of kerogen	0.21	υ_k	–
Mean radius of kerogen pockets	0.76	R_k	m
Initial kerogen porosity	0.1	ϕ_{k0}	–
Initial kerogen apparent permeability	1.2×10^{-21}	k_{k0}	m^2
Initial kerogen tortuosity	2.0	τ_{k0}	–
Biot coefficient of kerogen	0.4	α_k^*	–
Archie cementation index of kerogen	5	q_k	–
Characteristic contact area for *KTP*	SRD: 1.8×10^{-10} NSRD: 2.0×10^{-10}	$A_c^{*SRD} A_c^{*NSRD}$	m^2 m^2
Characteristic contact angle for *KTP*	SRD: 18 NSRD: 15	θ_{effc}^{SRD} θ_{effc}^{NSRD}	° °
Gas-water interfacial tension	SRD: $1.1 \times \gamma_{g-w}^{NSRD}$ NSRD: Interpolation based on the data in Fig. 6	γ_{g-w}^{SRD} γ_{g-w}^{NSRD}	N/m N/m
Bulk modulus of IM	7.25×10^9	K_m	Pa
Poisson's ratio of IM	0.2	υ_m	–
Mean length of IM blocks	3.05	L_m	m
Initial IM absolute permeability	1.0×10^{-20}	k_{m0}	m^2
Initial IM porosity	0.04	ϕ_{m0}	–
Initial IM tortuosity	1.5	τ_{m0}	–
Biot coefficient of IM	0.5	α_m^*	–
Initial water saturation in IM	0.26	S_{wm0}	–
Irreducible water saturation in IM	0.22	S_{wrim}	–
Irreducible gas saturation in IM	0.2	S_{grim}	–
Entry pressure for two-phase flow in IM	5.0×10^6	p_{em}	Pa
Archie cementation index of IM	2.5	q_m	–
Volumetric fraction of NA	0.07	η_{na}	–
Poisson's ratio of NA	0.27	υ_{na}	–
Biot coefficient of NA	1	α_{na}^*	–
Irreducible water saturation in NA	0.15	S_{wrina}	–
Irreducible gas saturation in NA	0.1	S_{grina}	–
Bulk modulus of NA	SRD: 4.0×10^8 NSRD: 2.0×10^9	K_{na}^{SRD} K_{na}^{NSRD}	Pa Pa
Initial NA porosity	SRD: 0.2 NSRD: 0.12	ϕ_{na0}^{SRD} ϕ_{na0}^{NSRD}	– –
Initial NA absolute permeability	SRD: 7.0×10^{-16} NSRD: 3.0×10^{-17}	k_{na0}^{SRD} k_{na0}^{NSRD}	m^2 m^2
Initial water saturation in NA	SRD: 0.8 NSRD: 0.4	S_{wna0}^{SRD} S_{wna0}^{NSRD}	– –
Entry pressure for two-phase flow in NA	SRD: 1.0×10^6 NSRD: 2.0×10^6	p_{ena}^{SRD} p_{ena}^{NSRD}	Pa Pa
Bulk modulus of HF	3.3×10^8	K_f	Pa
Biot coefficient of HF	1	α_f^*	–
Initial HF porosity	0.3	ϕ_{f0}	–
Initial HF absolute permeability	5.0×10^{-14}	k_{f0}	m^2
Initial HF aperture	0.003	b_{f0}	m
Initial water saturation in HF	0.8	S_{wf0}	–
Irreducible water saturation in HF	0	S_{wrif}	–
Irreducible gas saturation in HF	0	S_{grif}	–
Entry pressure for two-phase flow in HF	0	p_{ef}	Pa

is found that the proposed model in this work performs better than the single-phase flow model in matching the data of this case. Specifically, the single-phase flow model gives apparently higher daily gas production values than the field data during the first 10 days because it ignores the hindrance effect of water on gas flow, while the results computed by using the model proposed in this work are closer to the field data [see Fig. 10**(b)**]. Moreover, the single-phase flow model gives slightly lower daily gas production values compared to the field data during 1300 – 1700 day, while the results given by the proposed model excellently match the field data in this period. This difference can be ascribed to the combined effects of the on/off gas-supplying mechanism of kerogen and the two-phase flow. These effects are included in our model, while they are not considered in the single-phase flow model. For daily water production, the results simulated by using another two-phase flow model proposed by Cao et al. [14] for the same case during 1700 days are plotted in Fig. 10**(c)** for comparison. Furthermore, to show more details about the early stage of the water extraction process, the simulation results of the two models during the first 200 days are also particularly shown in Fig. 10**(d)**. It can be seen that the model proposed in this work gives very similar results compared to the results of Cao et al.'s model, which demonstrates the reliable performance of our model. It is noteworthy that our model incorporates more influencing factors (such as mechanical deformation and the on/off gas-supplying mechanism of kerogen) than Cao et al.'s model. As discussed below, the multiple influencing factors and complexities included in the proposed model may greatly affect the accuracy of reservoir production evaluation. In short, by the comparison presented in this section, the validity and applicability of the proposed multidomain, multiphysics, and two-phase flow model are verified.

As for the efficiency of our model, we used a laptop with an i7-7700HQ CPU (4 cores, 2.80 GHZ for each) and 32 GB RAM to run the model by using COMSOL Multiphysics in a 64-bit WIN 10 operating system. It took approximately 9 min to complete the simulation of the 1700-day gas and water extraction process for the Barnett Shale case. The geometry shown in Fig. 9**(d)** with 761 nodes and 1397 triangle elements was simulated. By using our model, it usually takes 50 – 100 min to complete a 30-year (this time period is sufficient to cover the industrial lifespan of a shale gas reservoir) gas and water production process in a shale reservoir. This shows the satisfactory efficiency of our model in which comprehensive and complex physical processes are integrated. However, it should be pointed out that the actual computation time to run a specific case is also affected by many factors including initial and boundary conditions, settings of the solver, quality of the mesh, number of the nodes, etc.

5. Results and discussion

In this section, a base case is first simulated to understand the general evolutions of key reservoir properties and gas/water production. The influences of the initial absolute permeabilities and bulk moduli of different components of the shale reservoir on the gas extraction process are investigated to highlight the importance of gas-supplying capability

of different media, mechanical coupling effect, and multi-domain effect for gas production (Section 5.1). After that, a sensitivity analysis focusing on the effects of water in the stimulated shale reservoir on gas production is carried out. This issue includes two aspects: (1) The effects of water on the gas–water-two-phase flow, which is influenced by the relative permeability curves (Section 5.2); (2) The effects of water on the liberation of the gas originally stored in kerogen, which is controlled by the on/off gas-supplying mechanism and *KTP* (Section 5.3). The findings and analysis in this section not only enhance the understanding of the gas–water-two-phase flowback process but also provide some insights into how to improve shale gas recovery.

5.1. Overview of shale gas extraction process: A base case

5.1.1. Overall gas/water flowback process

A base case is simulated by using the proposed multidomain, multiphysics, two-phase flow model to comprehensively understand the overall production behaviour of the stimulated shale gas reservoir containing water. The base case is adapted from the simulation case of Barnett Shale in Section 4, and its reservoir properties and modelling parameters are listed in Table 2. By comparing Table 1 and Table 2, it can be known that the base case has the following differences compared to the Barnett Shale case: (1) η_k and V_L are increased to have a higher original gas reserve in kerogen; (2) k_{k0}, k_{m0}, and k_{na0}^{SRD} are increased, and R_k is decreased to accelerate the gas extraction process (to avoid a too long simulation period of time needed for extracting all the recoverable gas); (3) S_{wm0} is increased to have more fluid fraction influenced by the on/off mechanism caused by water film; (4) A_c^{*SRD} and A_c^{*NSRD} are decreased, while θ_{effc}^{SRD} and θ_{effc}^{NSRD} are increased to get higher *KTP*s in SRD and NSRD. These modifications aim at forming a stimulated shale gas reservoir where the effect of the on/off gas-supplying mechanism on gas production is significant, while the reservoir parameters and the simulated gas/water flow rates are still in reasonable ranges. For the base case, an 80-year (29200-day) simulation of shale gas extraction is conducted. It took approximately 4 h to complete the 80-year simulation of the base case by using the laptop mentioned previously (see Section 4). No extra setting is needed to achieve such a long-time simulation. The daily production ($P_{d,gas}$) and the cumulative gas production ($P_{c,gas}$) of the whole shale reservoir in extraction process are shown in Fig. 11**(a)**. It can be known that the $P_{d,gas}$ exhibits a dual-peak behaviour. In the very beginning (1–5 day) of the production process, $P_{d,gas}$ sharply increases to exhibit the first gas production peak (approximately 1.3×10^5 standard m^3), then it drops considerably during 5–80 day. After that, $P_{d,gas}$ climbs up again until approximately 500 day to reach the second gas production peak (approximately 7.1×10^4 standard m^3), then it decreases again. Meanwhile, the $P_{c,gas}$ keeps climbing before it levels out at approximately 15000 day. The first peak of the $P_{d,gas}$ vs. time curve is narrow and high, which can be ascribed to the rapid depletion of the gas near the wellbore driven by the enormous pressure gradient between the bottom hole and the reservoir. In contrast, the second peak of the $P_{d,gas}$ vs. time curve is relatively wide and low, which is caused by the compensation effect of gas supply from kerogen. This dual-peak behaviour of $P_{d,gas}$ in stimulated shale reservoir has been reported by Shaoul et al. [63]. As for water production, the $P_{d,water}$ and the cumulative water production ($P_{c,water}$) curves are shown in Fig. 11**(b)**. $P_{d,water}$ soars to a significant peak at the very beginning of the production process, and then rapidly declines. Correspondingly, the $P_{c,water}$ curve first increases, and levels out at approximately 6000 day when the water can hardly be extracted. The general trend of water production simulated by using the proposed model is consistent with the results published in previous studies [14,64].

To further understand the water transport in the shale reservoir during gas extraction, the evolutions of S_{wna} and S_{wm} in SRD and NSRD are investigated. Besides, the change of S_{wf} is also studied. Three inspection points with their coordinates marked in Fig. 12 represent the

Table 2
Reservoir properties and modelling parameters for the base case.

Parameter	Value	Symbol	Unit
Simulation model dimension: length × width × thickness	30.48 × 145 × 90	–	m × m × m
Simulated SRD dimension: length × width × thickness	30.48 × 54.8 × 90	–	m × m × m
Half length of HF	47.2	–	m
Reservoir temperature	353.15	T	K
Number of HFs	28	N	–
Maximum horizontal geo-stress	41.6×10^6	–	Pa
Minimum horizontal geo-stress	37.3×10^6	–	Pa
Initial pore pressure of reservoir	20.34×10^6	p_{k0}, p_{m0}, p_{na0}, and p_{f0}	Pa
Bottom-hole pressure	3.69×10^6	BHP	Pa
Shale density	2460	ρ_s	kg/m^3
Molar weight of methane	0.016	M	kg/mol
Gas viscosity	1.84×10^{-5}	μ_g	Pa•s
Water density	971.8	μ_w	kg/m^3
Langmuir volume constant	0.005	V_L	m^3/kg
Langmuir strain constant	0.008	ε_L	–
Volumetric fraction of kerogen	0.12	η_k	–
Bulk modulus of kerogen	5.0×10^9	K_k	Pa
Poisson's ratio of kerogen	0.21	υ_k	–
Mean radius of kerogen pockets	0.5	R_k	m
Initial kerogen porosity	0.1	ϕ_{k0}	–
Initial kerogen apparent permeability	1.2×10^{-21}	k_{k0}	m^2
Initial kerogen tortuosity	2.0	τ_{k0}	–
Biot coefficient of kerogen	0.4	α_k^*	–
Archie cementation index of kerogen	5	q_k	–
Characteristic contact area for *KTP*	SRD: 1.8×10^{-13} NSRD: 3.0×10^{-12}	$A_c^{*SRD} A_c^{*NSRD}$	m^2 m^2
Characteristic contact angle for *KTP*	SRD: 60 NSRD: 45	θ_{effc}^{SRD} θ_{effc}^{NSRD}	° °
Gas-water interfacial tension	SRD: $1.25 \times \gamma_{g-w}^{NSRD}$ NSRD: Interpolation based on the data in Fig. 6	γ_{g-w}^{SRD} γ_{g-w}^{NSRD}	N/m N/m
Bulk modulus of IM	7.25×10^9	K_m	Pa
Poisson's ratio of IM	0.2	υ_m	–
Mean length of IM blocks	3.05	L_m	m
Initial IM absolute permeability	1.0×10^{-20}	k_{m0}	m^2
Initial IM porosity	0.04	ϕ_{m0}	–
Initial IM tortuosity	1.5	τ_{m0}	–
Biot coefficient of IM	0.5	α_m^*	–
Initial water saturation in IM	0.34	S_{wm0}	–
Irreducible water saturation in IM	0.22	S_{wrim}	–
Irreducible gas saturation in IM	0.2	S_{grim}	–
Entry pressure for two-phase flow in IM	5.0×10^6	p_{em}	Pa
Archie cementation index of IM	2.5	q_m	–
Volumetric fraction of NA	0.05	η_{na}	–
Poisson's ratio of NA	0.27	υ_{na}	–
Biot coefficient of NA	1	α_{na}^*	–
Irreducible water saturation in NA	0.15	S_{wrina}	–
Irreducible gas saturation in NA	0.1	S_{grina}	–
Bulk modulus of NA	SRD: 4.0×10^8 NSRD: 2.0×10^9	K_{na}^{SRD} K_{na}^{NSRD}	Pa Pa
Initial NA porosity	SRD: 0.2 NSRD: 0.12	ϕ_{na0}^{SRD} ϕ_{na0}^{NSRD}	– –
Initial NA absolute permeability	SRD: 7.0×10^{-16} NSRD: 3.0×10^{-17}	k_{na0}^{SRD} k_{na0}^{NSRD}	m^2 m^2
Initial water saturation in NA	SRD: 0.8 NSRD: 0.4	S_{wna0}^{SRD} S_{wna0}^{NSRD}	– –

(*continued on next page*)

Table 2 (*continued*)

Parameter	Value	Symbol	Unit
Entry pressure for two-phase flow in NA	SRD: 1.0×10^{6}	p_{ena}^{SRD}	Pa
	NSRD: 2.0×10^{6}	p_{ena}^{NSRD}	Pa
Bulk modulus of HF	3.3×10^{8}	K_f	Pa
Biot coefficient of HF	1	α_f^*	–
Initial HF porosity	0.3	ϕ_{f0}	–
Initial HF absolute permeability	5.0×10^{-14}	k_{f0}	m^2
Initial HF aperture	0.003	b_{f0}	m
Initial water saturation in HF	0.8	S_{wf0}	–
Irreducible water saturation in HF	0	S_{wrif}	–
Irreducible gas saturation in HF	0	S_{grif}	–
Entry pressure for two-phase flow in HF	0	p_{ef}	Pa

different domains of the reservoir: Point A represents HF, Point B denotes SRD, and Point C represents NSRD, respectively. The evolutions of water saturations at these three points with the time elapsed during 7300-day production are shown in Fig. 13. The water saturation curves can be divided into three groups: (1) S_{wf} andS_{wna}^{SRD}. They have high values and extremely similar trends. This is due to the high water contents near the wellbore caused by the invasion of the fracking fluid and the great capability of SRD to supply fluids to the wellbore. Note that the HF only occupies a very small volume of the reservoir. After the gas extraction starts, the water and gas originally in HF deplete in several days. In subsequence, NA-SRD (with high permeability) effectively supplies fluids to HF to compensate for the extracted fluids, which dominates the evolution of water saturation in HF in the most time of production. Thus, the highly similar trends of the water saturations in HF and SRD are seen. (2)S_{wna}^{NSRD}. The mass transfer in NSRD is the consequence of the complex coupling interactions between different media and domains. As a part of the natural fractures system of the stimulated shale reservoir, NA-NSRD is not only connected with NA-SRD, but also linked with IM. The moderate increase of S_{wna}^{NSRD} during shale gas extraction shown in Fig. 13 can be deemed as a water re-distribution process under the fully coupled multidomain and multiphysical effects. Note that although the S_{wna}^{NSRD} increases with time, the net trend of the water storage in the whole reservoir always decreases because both the S_{wna}^{SRD} and S_{wm} are dropping in the meantime to offset the increase ofS_{wna}^{NSRD}. (3) S_{wm} at Point B and Point C. Because of the much lower permeability of IM compared to that of NA subsystem, the water transport in IM is slow. More specifically, the decrease of S_{wm} at Point C (far from the HF) is slower than that at Point B (close to the HF). These results reveal that the general mass transfer trends in different media and domains are complicated. Previously, Cao et al. [14] and Cui et al. [22] proposed their gas–water-two-phase flowback models to simulate the gas–water extraction process. However, their models cannot predict some trends in the production process, such as the increase ofS_{wna}^{NSRD}, because they employed the dual-porosity (organic + inorganic) system instead of the triple-porosity (kerogen + IM + NA) system and do not comprehensively incorporate the property differences between SRD and NSRD into their models. For example, Cao et al.'s model does not consider the effect of shale deformation in different domains, while Cui et al.'s model does not incorporate the difference of initial and irreducible water saturations between NA-SRD and NA-NSRD caused by hydraulic fracking. Therefore, the model proposed in this work has its advantages in fulfilling more accurate and finer simulations. In the following text, the effects of various parameters on shale gas production are investigated as the key responses because gas recovery is the top concern for the industry. The evolutions of some other important properties including water production and absolute/relative permeabilities are also briefly discussed.

5.1.2. *Effects of initial permeabilities on shale gas production*

Initial absolute (apparent) permeabilities of different components of the shale reservoir affect gas production. Many previous studies have been discussed these effects [4,12,13,14,22,30,63,64,65]. Here, we first focus on an interesting issue, i.e., the dual-peak behaviour of daily gas production exhibited in Fig. 11**(a)**. The previously published studies have suggested that in some cases, the daily gas production shows the dual-peak behaviour, while in other cases, it appears a single-peak behaviour, just like Fig. 10 displays. This difference in the shape of the daily gas production curve from case to case is dependent on the contrast of the mass-supplying abilities of different porous media in the shale reservoir. To understand this opinion, the effects of initial apparent (absolute) permeabilities of kerogen (k_{k0}) and IM (k_{m0}) on $P_{d,gas}$ are studied based on the base case. As shown in Fig. 14**(a)**, the second peak of the daily gas production curve becomes smaller with the decrease of k_{k0}. Conversely, a higher k_{k0} makes the second peak higher and wider. When the k_{k0} is very low, the second peak is negligible. Consequently, the daily production curve becomes single-peak. For instance, the daily production curve for $k_{k0} = 1 \times 10^{-21}$ m^2 has a similar (single-peak) shape to that of the field case of Barnett Shale [see Fig. 10 **(a)**]. Obviously, k_{k0} reflects the ability of kerogen to supply gas to IM, which controls the shape of the daily production curve. If the gas supplying rate from kerogen to IM is slow, the daily production curve tends to be single-peak. Otherwise, the daily production curve is dual-peak. On the other hand, for the effect of k_{m0} on daily gas production, it can be known from Fig. 14**(b)** that the higher k_{m0} significantly enhances the early-period daily production curve, especially the height of the first peak. Nevertheless, decreasing k_{m0} does not change the dual-peak daily production curve to a single-peak curve. With the elapse of time, the enhancing effect of increasing k_{m0} on daily gas production diminishes. Therefore, it can be concluded that both k_{k0} and k_{m0} significantly influence daily gas production in the early period. The former mainly influences the shape of the daily production curve (especially the shape of the second peak), while the latter comprehensively affects the early-period daily gas production. This is essentially determined by the contrast of the fluid-supplying abilities of kerogen and IM.

The effects of k_{k0} and k_{m0} on cumulative gas production are presented in Fig. 15. As seen in Fig. 15**(a)**, the effect of k_{k0} on cumulative gas production varies during the whole production period. In the early period (0–4000 day), the higher k_{k0} corresponds to the higher cumulative gas production curve. This is ascribed to the enhanced early-period daily gas production, as mentioned above. With the gas extraction going on, the order of the curves with different k_{k0}s gradually reverses. At the end of the gas extraction, the highest k_{k0} corresponds to the lowest cumulative production. This reveals that if the k_{k0} is too high, the gas supply from kerogen in the early period will be so fast that some kerogen pockets turn off early. As a result, some original gas in place is sealed in kerogen permanently. This phenomenon, controlled by the on/off gas-supplying mechanism of kerogen with water film, will be discussed in **Section 5.3**. On the other hand, it can be known from Fig. 15**(b)** that the higher k_{m0} leads to the earlier completion of gas extraction (which is symbolized by the level out of the cumulative gas production), and the final cumulative gas productions with different k_{m0}s are nearly identical. This suggests that k_{m0} only affects the speed of gas extraction, while does not influence the ultimate gas recovery because the on/off gas-supplying mechanism is not applied on IM.

The effects of initial permeabilities of NA-SRD (k_{na0}^{SRD}) and NA-NSRD (k_{na0}^{NSRD}) on daily gas production are presented in Fig. 16. It can be known from Fig. 16**(a)** that a high k_{na0}^{SRD} significantly enhances the early-period daily gas production and makes the shape of the daily gas production curve convert from dual-peak into single-peak. However, this enhancing effect of increasing k_{na0}^{SRD} on daily gas production disappears early. For instance, the daily gas production with $k_{na0}^{SRD} = 4 \times 10^{-16}$ m^2 is the highest one in the curve group in Fig. 16**(a)** in the early period, but it is exceeded by those with the lower k_{na0}^{SRD} s after 1700 days. From Fig. 16 **(b)**, it can be seen that the enhancing effect of increasing k_{na0}^{NSRD} on the early-period daily gas production is not so strong as that caused by increasingk_{na0}^{SRD}, but this effect lasts for a longer period of time (0–3650 day). Furthermore, the effects of k_{na0}^{SRD} and k_{na0}^{NSRD} on cumulative gas

production are shown in Fig. 17. Although the NA subsystem only occupies 5% (by volume) of the reservoir, increasing either k_{na0}^{SRD} [see Fig. 17**(a)**] or k_{na0}^{NSRD} [see Fig. 17**(b)**] greatly improves the gas extraction speed. This can be ascribed to the great connectivity and high permeability of the NA subsystem. Increasing the initial absolute permeability of either NA-SRD or NA-NSRD causes a higher differential pressure between NA and IM, which intensifies the mass exchange. By comparing Fig. 17**(a) and (b)**, it can be known that the extraction-accelerating effect caused by increasing k_{na0}^{SRD} happens much earlier than that caused by increasingk_{na0}^{NSRD}, which is reflected by the enormous difference between the daily gas production curves in the earlier period in Fig. 17**(a)**. The reason is that the fluids in SRD start flowing out earlier than that in NSRD. These results indicate the importance of NA subsystem for gas extraction from shale reservoirs. In engineering practice, the hydraulic fracking treatment directly improves the initial absolute NA permeability by creating numerous secondary hydraulic fractures and activating the original natural fissures in the scope of SRD, which is one of the most effective ways to enhance gas production. Obviously, the triple-porosity-multidomain model proposed in this work helps obtain accurate and fine simulation results by considering the NA subsystem as an individual continuum and differentiating SRD/NSRD so that the impact of the difference between matrix/fracture and the discrepancy in different domains can be reflected.

5.1.3. Effects of bulk volumetric moduli on shale gas production

The bulk volumetric modulus of a continuum is inversely proportional to the pore compressibility [4,40,41,23]. Therefore, it affects the evolution of the stress-dependent porosity of shale, which further influences the stress-dependent permeability and gas production. Moreover, the effects caused by the change of bulk modulus may have effects on different domains since the shale deformation is solved by a globally coupled equation [Eq.]. Based on the base case, the effects of NA-SRD bulk modulus (K_{na}^{SRD}) on the gas extraction process are investigated, as shown in Fig. 18. The cumulative gas productions with different K_{na}^{SRD} s in 29200-day shale gas extraction are shown in Fig. 18**(a)**. The higher bulk modulus of NA-SRD corresponds to the higher gas extraction rate because it means the smaller mechanical shrinkage during gas depletion. Thus, the closure of natural fractures is slighter, and the reduction of the stress-dependent permeability of NA-SRD ($k_{na,stress}^{SRD}$) is slighter, which benefits gas recovery. Another interesting issue is the multidomain effects of mechanical deformation. Changing K_{na}^{SRD} not only varies the evolution of stress-dependent permeability of NA-SRD [$k_{na,stress}^{SRD}$, as shown in Fig. 18**(b)**], but also leads to different permeability evolutions in other domains (e.g., $k_{na,stress}^{NSRD}$ and $k_{f,stress}$), as seen in Fig. 18**(c) and (d)**. This can be ascribed to the mechanical coupling interactions between different domains. Specifically, both $k_{na,stress}^{NSRD}$ and $k_{f,stress}$ decrease more intensively with the increase ofK_{na}^{SRD}, which can be deemed as a harmonic result of the whole shale reservoir by the mechanical coupling relation. With the decrease of SRD compressibility caused by the increase ofK_{na}^{SRD}, the deformations in NSRD and HF correspondingly increase to fulfill a mechanical equilibrium under the in-situ stress condition [4]. Also, the influences of NA-NSRD bulk modulus (K_{na}^{NSRD}) on the gas extraction process are investigated, as shown in Fig. 19. It can be known that increasing K_{na}^{NSRD} improves the extraction speed [see Fig. 19**(a)**] and alleviates the shrinkage-induced reduction of $k_{na,stress}^{NSRD}$ [see Fig. 19**(b)**], but the effects on the permeability evolutions in other domains are negligible [see Fig. 19**(c) and (d)**]. In brief, the effects of changing bulk moduli of natural fractures network are different in various domains. In engineering practice, K_{na}^{SRD} usually differs from K_{na}^{NSRD} due to stimulation treatments (e.g., hydraulic fracking). Therefore, the mechanical coupling interactions between different domains with various mechanical properties should be taken into consideration in shale reservoir simulation to obtain accurate results.

5.2. Effects of relative permeability on flowback process

For the gas–water-two-phase flowback process, an important issue is the effects of gas and water relative permeabilities because these relative permeabilities directly affect the mobility of each phase. We varied the irreducible water saturation of NA-SRD (S_{wrina}^{SRD}) to obtain a series of relative permeability curves, and then investigated the effects of these relative permeability curves on the gas and water productions in 7300-day production based on the base case, as shown in Fig. 20. According to **Appendix 3C**, the gas/water relative permeability curves based on the Brooks and Corey's model with different irreducible water saturations of NA-SRD (S_{wrina}^{SRD} s) are shown in Fig. 20**(a)**. Note that both water and gas relative permeability curves change withS_{wrina}^{SRD}. With the increase ofS_{wrina}^{SRD}, both gas and water phases become difficult to flow, which is reflected by the narrowing down of the two-phase zone in Fig. 20**(a)**. Based on the base case, the simulated variations of gas/water relative permeabilities of NA-SRD at Point B during 7300-day production are presented in Fig. 20**(b)**. The relative permeability variations mainly occur in the first 400 days, so the resultant effects on production appear in the early period. It can be known from Fig. 20**(c)** that the effect of S_{wrina}^{SRD} on cumulative gas production can be ignored. This is because at the beginning of gas extraction, most of the fluid stored in NA-SRD is water. The high initial water saturation of NA-SRD means that the amount of gas affected by the change of S_{wrina}^{SRD} is small, which results in the negligible effect of S_{wrina}^{SRD} on gas production. However, the higher S_{wrina}^{SRD} leads to considerable reduction of cumulative water production, as shown in Fig. 20**(d)**. This effect appears in the early period of production (0–500 day). The high content of water in NA-SRD implies that the shapes of relative permeability curves are important to control the water mobility in this domain and affect the overall water flowback. With the increase ofS_{wrina}^{SRD}, the water retention in SRD becomes higher. That is, recoverable water becomes less. Hence, cumulative water production is greatly curtailed, which can be deemed as a kind of formation damage related to the wettability alteration of the reservoir rock [14,51,66,67]. These results suggest that although the NA subsystem only occupies a small fraction of the reservoir volume (e.g., 5%, see Table 2), the relative permeabilities of NA-SRD are of importance for water recovery. Some undesirable effects caused by the invasion of external fluids may lead to the wettability alteration of the reservoir rock in SRD. This is partly reflected by the increase ofS_{wrina}^{SRD}, which negatively affects water recovery. This effect may be vital in many engineering cases where high water recovery is desired because the fracking fluids need to be recovered as much as possible [68,69].

In the fracking process, IM imbibition (caused by the hydrophilic feature of the IM pores) occurs as another consequence of external fluid invasion, which increases the initial IM water saturation. Due to the extremely small pore size of IM, the imbibition effect driven by the high IM capillary pressure is usually strong [11,14]. Once gas production starts, some water in IM may be extracted, which depends on the movable amount of water in IM. It is necessary to study the influence of relative permeabilities of IM on gas/water production because IM takes a large fraction of reservoir volume (e.g., 83%, see Table 2). We changed the irreducible water saturation of IM (S_{wrim}) to obtain a series of IM relative permeability curves, and then investigated the effects of these relative permeability curves on the gas and water production in 7300 days based on the base case, as shown in Fig. 21. The gas/water relative permeability curves based on Brooks and Corey's model with different S_{wrim}s are shown in Fig. 21**(a)**. With the increase of S_{wrim}, both gas and water become difficult to flow, which is reflected by the narrowing down of the two-phase zone in Fig. 21**(a)**. The simulated evolutions of the IM relative permeabilities of gas and water at Point B of the base case are plotted in Fig. 21**(b)**. The variation of the IM relative permeabilities during shale gas extraction is slow, but it lasts a longer time compared to that in NA-SRD. This long-term variation is the combined result of the

extremely low IM absolute permeability (which leads to the slow change of IM water saturation, and thus, the slow change of IM relative permeabilities) and the large volume fraction of IM in the shale reservoir (which leads to the long-term change of IM relative permeabilities). In consequence, the shale reservoir with a higher S_{wrim} (meaning higher water retention) has lower cumulative gas and water productions [Fig. 21**(c) and (d)**]. Note that this production-hindering effect caused by the increase of S_{wrim} does not appear in the first 1000 days because the early-period production is mainly related to the NA instead of the IM. With the elapse of time, the supply of fluids in IM becomes increasingly important. Thus, the hindering effect of the high S_{wrim} (i.e., the fewer amount of movable water) on gas and water production can be seen. These results indicate that the change of S_{wrim} influences the long-term mass transport process in the shale reservoir to some degree. Due to the imbibition effect, external fluids may invade into IM to alter the wettability and negatively affect gas and water production. This investigation demonstrates the importance of ensuring the compatibility of working fluids (fracking/drilling/completion fluids) with shale formation wettability to avoid formation damage.

5.3. Effects of on/off gas-supplying mechanism of kerogen on shale gas extraction

The on/off gas-supplying mechanism of kerogen introduced in this work establishes the linkages of the differential pressure between kerogen and inorganic matrix, the properties of the heterogeneous interface, and dynamic kerogen porosity. The proposed multidomain numerical computation tool allows individually setting the parameters related to the on/off gas-supplying mechanism in SRD and NSRD so that the different performances of this mechanism in different domains can be reflected. To understand the effects of the on/off gas-supplying mechanism on gas extraction, five cases representing different wetting conditions at the heterogeneous interface of kerogen are simulated by using the proposed model based on the base case. The involved parameters are listed in Table 3. We use the different parameter combinations instead of changing a single parameter to obtain a series of *KTP* values to represent the different degrees of formation damage caused by wettability alteration because these parameters are closely associated with each other. For example, the lower gas–water interfacial tension usually leads to the lower contact angle and the larger contact area [51]. Here, Case 1 represents the situation without the consideration of the on/off gas-supplying mechanism, which is fulfilled by setting the *KTP* as zero in the whole reservoir, that is, the kerogen pockets with water film can supply gas to IM without the restriction of additional differential pressure threshold. Cases 2, 3, and 4 represent the different formation damage/stimulation occasions. In these three cases, the wettability parameters of NSRD are identical, while those of SRD are different from one case to another. Case 3 is the base case mentioned above. It describes moderate formation damage in SRD caused by the invasion of fracking fluids. Specifically, SRD has higher gas–water interfacial tension (γ_{g-w}^{SRD}), higher characteristic contact angle (θ_{effc}^{SRD}), and larger characteristic contact area (A_c^{*SRD}) than those of NSRD (γ_{g-w}^{NSRD},θ_{effc}^{NSRD}, and A_c^{*NSRD}). Case 2 is a wettability-enhanced case in which the SRD wettability parameters lead to a lower *KTP* (i.e., the kerogen is easier to supply gas) than that of Case 3. Specifically, SRD has lower gas–water interfacial tension (γ_{g-w}^{SRD}), lower characteristic contact angle (θ_{effc}^{SRD}), and smaller characteristic contact area (A_c^{*SRD}) than those of NSRD (γ_{g-w}^{NSRD},θ_{effc}^{NSRD}, and A_c^{*NSRD}). Conversely, Case 4 describes a severely damaged SRD in which an obtuse contact angle is seen caused by the undesirable wettability alteration. This may result from the effect of the invasion of the incompatible surfactants in fracking fluids [51,66,69]. In Case 5, all the gas in kerogen with water film is sealed, which is fulfilled by simply modifying the expression of the sink term of kerogen [Eq.] to the following form which excludes the gas supply from those kerogen pockets with water film:

$$Q_{k-m} = \frac{D_{k-m}\rho_{gk}k_{kapp}S_{gm}}{\mu_g}(p_k - p_m) \tag{59}$$

This sink term only includes the gas supply from those kerogen pockets without water film which is not influenced by the sealing effect of water, while the kerogen pockets with water film have no contribution to mass transfer. The long-term gas production performances of these cases in 29200-day (80-year) extraction are shown in Fig. 22. It can be seen from Fig. 22**(a)** that different interfacial/surface properties related to formation damage result in a significant difference in cumulative productions. Specifically, if the on/off gas-supplying mechanism is ignored (Case 1), the final cumulative production (2.01×10^8 standard m^3) is 35.3% higher than that of the reservoir where all kerogen pockets with water film are closed (1.56×10^8 standard m^3, Case 5), and 19.2% higher than that of the reservoir severely damaged (1.77×10^8 standard m^3, Case 4). The recoveries of the original gas in kerogen of these five cases during the 29200-day extraction are presented in Fig. 22**(b)**, indicating that the ultimate gas recovery of Case 1 is 47.8% higher than that of Case 5 and 21.4% higher than that of Case 4. Obviously, this difference is originated from the on/off mechanism controlled by *KTP* reflecting the combined effect of seepage, kerogen wettability, and shale deformation. The numerically computed *KTP*s in different domains for Cases 1 – 4 during extraction are shown in Fig. 23. It can be known from Fig. 23**(a)** that the *KTP*s in SRD significantly vary with the different wetting conditions. For Case 1, there is no sealing effect of water on kerogen, so the *KTP* is always zero in both SRD and NSRD. With the severe formation damage (Case 4), the kerogen in SRD has a considerable *KTP* (approximately 0.42 MPa). The moderately damaged formation (Case 3) has a moderate *KTP* in SRD (approximately 0.05 MPa), while the wettability-enhanced formation (Case 2) has a low *KTP* in SRD (approximately 7.6×10^{-4} MPa). On the other hand, Cases 2, 3, and 4 have very similar *KTP*s in NSRD [approximately 0.025 MPa, as shown in Fig. 23**(b)**] since the external fluids do not affect NSRD. Here, it must be pointed out that the *KTP*s in Fig. 23 are not constant except that of Case 1 (zero), although their variation with time is slight. This is because that the *KTP* expression includes the stress-dependent kerogen porosity changing with the gas depletion [see Eq.].

To further understand the control of *KTP*-based on/off mechanism on

Table 3
Five simulation cases representing different wetting conditions at the heterogeneous interface of kerogen.

Case number	Variable settings		Meaning
	SRD	NSRD	
1	$KTP = 0$		The on/off gas-supplying mechanism is not considered (the kerogen is all-open)
2	$A_c^{*SRD} = 5.0 \times 10^{-9}$ m^2 $\theta_{effc}^{SRD} = 18^\circ$ $\gamma_{g-w}^{SRD} = 0.5\times\gamma_{g-w}^{NSRD}$	$A_c^{*NSRD} = 3.0 \times 10^{-12}$ m^2 $\theta_{effc}^{NSRD} = 45^\circ$ γ_{g-w}^{NSRD} is based on interpolating the data in Fig. 6	The SRD is wettability-enhanced
3	$A_c^{*SRD} = 1.8 \times 10^{-13}$ m^2 $\theta_{effc}^{SRD} = 60^\circ$ $\gamma_{g-w}^{SRD} = 1.25\times\gamma_{g-w}^{NSRD}$		The SRD is moderately damaged (the base case)
4	$A_c^{*SRD} = 1.25 \times 10^{-14}$ m^2 $\theta_{effc}^{SRD} = 150^\circ$ $\gamma_{g-w}^{SRD} = 1.67\times\gamma_{g-w}^{NSRD}$		The SRD is severely damaged
5	Q_{k-m} is determined by Eq.		All of the kerogen pockets with water film are closed

gas liberation, we compare the differential pressure ($p_k - p_m$) curves and the *KTP* curves in SRD (Point B) of the shale reservoirs with different degrees of damage formation (Cases 2, 3, and 4), as shown in Fig. 24**(a), (b), and (c)**, respectively. It can be seen from Fig. 24**(a)** that the typical ($p_k - p_m$) curve goes up rapidly in the early period of gas extraction, and then significantly drops, exhibiting a large peak. After that, the ($p_k - p_m$) curve gradually levels out with the pressure depletion. This differential pressure is the driving force of the mass exchange between kerogen and IM. When $p_k - p_m = 0$, the mass exchange between kerogen and IM ends up, which means that the gas-supplying process of kerogen reaches the final equilibrium. In the early period of production, the value of ($p_k - p_m$) is high, so the gas in the kerogen pockets has sufficient energy to flow into IM. Once $p_k - p_m < KTP$ (about 7.6×10^{-4} for Case 2), the kerogen with water film will shut down. For the wettability-enhanced reservoir (Case 2), the shut-down time at Point B is at approximately 15000 day, which is sufficient for the kerogen with water film to release most of its gas reserve. For Case 3 [Fig. 24**(b)**], it has a higher *KTP* (around 0.05 MPa) than that of Case 2 due to the formation damage. This leads to an earlier intersection point of the decreasing part of the ($p_k - p_m$) curve and the *KTP* curve (marked by the blue circle). That is, the kerogen with water film shuts down earlier (at approximately 4000 day). For the severely damaged reservoir (Case 4) [Fig. 24**(c)**], the *KTP* is as high as 0.42 MPa. The value of ($p_k - p_m$) is lower than *KTP* in the whole production process. This means that the kerogen with water film at Point B in Case 4 is totally closed. It must be pointed out that this mechanism is only applied to the kerogen with water film, while those kerogen pockets without water film can still supply gas to IM. Therefore, although the kerogen with water film is closed, ($p_k - p_m$) still changes with time. An illustration summarizing the key information about the on/off mechanism is displayed in Fig. 24**(d)**. *KTP* is a compound indicator of a series of effects including seepage, wetting behaviour, and shale deformation on gas liberation. A high *KTP* is harmful to liberate gas from kerogen with water film because it lets the kerogen shut down early. As introduced in **Section 2.1**, *KTP* is considered as a physical and mathematical description of the activation energy barrier for breaking the sealing of water film to release gas from kerogen. The higher this activation energy barrier is, the more difficultly the kerogen releases gas. Another interesting issue revealed here is that under the control of the on/off gas-supplying mechanism, the shape of the ($p_k - p_m$) curve is also important for releasing gas. According to Fig. 24**(d)**, a high but narrow peak of the ($p_k - p_m$) curve is adverse for the long-term gas liberation from kerogen because the kerogen with water film will close too early. In contrast, if the peak of the ($p_k - p_m$) curve is low but wide, the long-term gas liberation from kerogen with water film may be significantly enhanced due to the longer opening time. This explains why in some engineering cases, after hydraulic fracking, the gas flow rate greatly increases in the early period of production, but it severely declines soon. Too intensive enhancement of production rate in a short term caused by inappropriate fracking operations may lead to a narrow peak of ($p_k - p_m$) curve, which makes the gas extraction non-sustainable [1]. Obviously, fracking operations must be carefully designed to create an optimized SRD with appropriately enhanced permeability and a suitable volume so that the gas can be extracted at a proper pace. Besides, it is demonstrated by these results that gas recovery can be enhanced by decreasing *KTP* (like Case 2) with the use of some surfactants, or by eliminating the formation damage (like Case 1) with the use of water-free fracking fluids (such as supercritical carbon dioxide, more details can be seen in the study proposed by Cao et al. [70]).

The evolutions of on/off state distribution of kerogen with water film in the whole simulated geometry (i.e., a half hydraulic fracking segment) for Cases 2, 3, and 4 during shale gas extraction are shown in Figs. 25, 26, and 27, respectively. In these figures, the on/off state of kerogen with water film is expressed by the value of the control function, i.e., $switch(p_k, p_m)$ given in Eq.. Specifically, red represents that the kerogen with water film is open [$switch(p_k, p_m) = 1$], while blue denotes that the kerogen with water film is closed [$switch(p_k, p_m) = 0$]. According to Fig. 25, the evolution of kerogen with water film for Case 2 (SRD is wettability-enhanced) can be divided into six periods: (1) At the beginning of gas extraction, the kerogen with water film near the bottomhole starts opening, and the scope of the opened kerogen pockets spreads from the SRD to the NSRD. (2) After 200 days, all the kerogen pockets are opened. This all-open state of the whole reservoir lasts until approximately 6500 day, then (3) the kerogen pockets with water film in the NSRD starts shutting down. The closed kerogen in NSRD first appears near the SRD/NSRD boundary and then gradually spreads towards the outer boundary of the NSRD. (4) At approximately 10000 day, all the kerogen pockets with water film in NSRD are shut down, while those in SRD are still open. This state lasts until approximately 13000 day. (5) After 13000 days, the kerogen pockets with water film in SRD start closing. The scope of the closed kerogen pockets spreads from the bottomhole to the SRD/NSRD boundary. (6) At 15370 day, all the kerogen pockets with water film in the reservoir are closed. This all-closed state remains until the end of gas extraction. On the other hand, the all-open state of the kerogen with water film in Case 3 (SRD is moderately damaged) lasts a shorter period (200 – 3500 day) than that in Case 2, and the all-close state starts earlier (at 9250 day) than that in Case 2. This is ascribed to the higher *KTP* in SRD of Case 3 compared to that of Case 2. Consequently, Case 3 obtains a lower ultimate gas recovery than that of Case 2, which has been indicated in Fig. 22. Furthermore, the all-open state of the kerogen with water film does not exist in Case 4 (SRD is severely damaged) because of the highest *KTP* in SRD in the three cases. In SRD, only a small fraction of the kerogen pockets with water film are opened for a short period (1–600 day), while others are never opened during the whole gas extraction process. In addition, the all-close state of Case 4 starts slightly earlier (at 9220 day) than that in Case 3. These directly lead to the lowest ultimate gas recovery of Case 4 in the three cases, as presented in Fig. 22. It is obvious that the formation-damage-induced wettability alteration is reflected by *KTP* which controls the gas liberation from the kerogen with water film and thereby affects the long-term gas recovery by the on/off mechanism. Lastly, this work proves that the effects of water on shale gas extraction include two aspects: (1) Two-phase flow in matrix and fractures, and (2) Sealing effect on gas in kerogen. The former affects the gas flow in inorganic matrix and fractures, while the latter (which is often neglected in the previous studies) influences the gas liberation from kerogen.

6. Conclusions

In this study, a fully coupled model considering water effects is developed to evaluate the gas–water-two-phase flowback process in gas extraction from stimulated shale reservoirs. The complexities of shale deformation and gas–water-two-phase flow in different domains of shale reservoirs are incorporated into the model. Especially, a concept of kerogen threshold differential pressure (*KTP*) is proposed to describe the effect of water on gas liberation from kerogen. *KTP* bridges the effects of seepage, wettability behaviour, and shale deformation, and it acts by an on/off mechanism. The proposed model was used to perform numerical simulations by using the finite element method and verified against field observations and results of previous studies. Based on the sensitivity analysis, the following findings can be obtained:

(1) The mechanical coupling interactions between different domains of the stimulated shale gas reservoir influence both early and long-term cumulative gas production. The change in pore compressibility in one domain affects the evolution of transport properties throughout the entire shale reservoir, which further influences gas production. In either the stimulated reservoir domain or the non-stimulated reservoir domain, a high bulk modulus of the natural fractures network benefits gas extraction by decreasing the shrinkage of flow channels during the process of pore pressure depletion.

(2) The single/dual peak behaviour of daily gas production is dependent on the contrast of gas-supplying capabilities of the different components in different domains of the stimulated shale reservoir.

(3) Water influences shale gas extraction in two aspects: One is the two-phase flow in inorganic matrix and fractures, the other is the sealing effect on the original gas in kerogen. The former influences the gas/water flow in inorganic matrix and fractures, while the latter controls the gas liberation from kerogen.

(4) The shapes of relative permeability curves of the natural fractures network in the stimulated reservoir domain considerably influence water production in the early period of shale gas extraction, while having little effect on gas production. The shapes of relative permeability curves of the inorganic matrix affect both gas and water cumulative productions from shale reservoirs. As a reflection of shale wettability, the shapes of these relative permeability curves may be influenced by formation damage.

(5) The properties related to shale wettability and interfacial behaviours, including contact angle, gas–water interfacial tension, and contact area, jointly affect the value of *KTP*, and further significantly influence ultimate gas production. The shale gas recovery can be enhanced by decreasing *KTP* by selecting appropriable surfactants of fracking fluids, or by using water-free fracking fluids (such as supercritical carbon dioxide).

(6) With the control of the on/off gas-supplying mechanism, the contrast between *KTP* and the kerogen-matrix differential pressure of the water-containing shale reservoir determines the shut-off time point to cease the gas supply from the kerogen with water film, and further influences the sustainability of shale gas extraction.

Declaration of Competing Interest

The authors declare that they have no known competing financial interests or personal relationships that could have appeared to influence the work reported in this paper.

Acknowledgements

The authors gratefully acknowledge the financial support from the Australian Government Research Training Program (RTP) scholarship and the Australian Research Council Grant No. DP200101293. Parts of this work have been completed to fulfill the Ph.D. degree requirements of Wai Li at the University of Western Australia.

Appendix

Appendix A:. Calculation of gas density in different media

For a given medium i ($i = k$ for kerogen; $i = m$ for IM; $i = na$ for NA, and $i = f$ for HF), the gas density ρ_{gi} can be calculated by using the real gas equation of state:

$$\rho_{gi} = \frac{M}{Z_i RT} p_{gi} \tag{A.1}$$

where M is the gas molar weight, 0.016 kg/mol; R is the universal gas constant, 8.314 J/(mol·K); T is the reservoir temperature; p_{gi} is the gas pressure in medium i. Z_i is the deviation factor of real gas in medium i, which is calculated by the empirical formula proposed by Mahmoud [71]:

$$Z_i = 0.702\left(p_{pri}\right)^2 \exp\left(-2.5T_{pri}\right) - 5.524p_{pri}\exp\left(-2.5T_{pri}\right) + 0.044\left(T_{pri}\right)^2 - 0.164T_{pri} + 1.15 \tag{A.2}$$

where $p_{pri} = p_{gi}/p_{cr}$ is a pressure ratio, p_{cr} is the critical pressure of methane, 4.6×10^6 Pa. $T_{pri} = T_i/T_{cr}$ is a temperature ratio, and T_{cr} is the critical temperature of methane, 190.74 K.

Appendix B:. Flow-regime effect and Knudsen number in kerogen and inorganic matrix

The general form of the flow-regime-dependent permeability enhancement function $f(Kn_i)$ of kerogen and IM ($i = k$ for kerogen and $i = m$ for IM) is proposed by the following equation [27,72,73]:

$$f(Kn_i) = (1 + \zeta_i Kn_i)\left(1 + \frac{4Kn_i}{1 + Kn_i}\right) \tag{B.1}$$

where Kn_i is the Knudsen number in medium i; ζ_i is a rarefaction coefficient in kerogen calculated by the following empirical formula:

$$\zeta_i = \frac{\zeta_0}{1 + \frac{A}{Kn_i^B}} \tag{B.2}$$

where ζ_0 is an asymptotic limit value; A and B are empirical coefficients. For an ultra-low permeability gas reservoir, $A = 0.178$; $B = 0.4348$; $\zeta_0 = 1.358$ [27]. These empirical coefficients have been shown valid for shale formations in many previous studies [4,73,74].

Kn_i is defined as:

$$Kn_i = \frac{\lambda_i}{r_{i,stress}} \tag{B.3}$$

where λ_i is the mean free path of a single gas molecule; $r_{i,stress}$ is the stress-dependent pore size of medium i. λ_i can be calculated according to the formula proposed by Civan et al. [73]:

$$\lambda_i = \frac{\mu_g}{p_{gi}}\sqrt{\frac{\pi Z_i RT}{2M}} \tag{B.4}$$

Similarly, in the initial state, we have the expressions of the initial Knudsen number (Kn_{i0}) and the initial mean free path of a single gas molecule (λ_{i0}):

$$Kn_{i0} = \frac{\lambda_{i0}}{r_{i0}} \tag{B.5}$$

$$\lambda_{i0} = \frac{\mu_g}{p_{gi0}}\sqrt{\frac{\pi Z_{i0} RT}{2M}} \tag{B.6}$$

where the r_{i0} is the initial pore size of medium i; Z_{i0} is the deviation factor of real gas in medium i. To determine the $r_{i,stress}$, we apply the Hagen-Poiseuille equation for a bundle of capillaries:

$$r_{i,stress} = \sqrt{\frac{8k_{i,stress}\tau_{i,stress}}{\phi_{i,stress}}} \tag{B.7}$$

where $\tau_{i,stress}$ is the stress-dependent tortuosity of medium i determined by the following equation:

$$\tau_{i,stress} = \frac{1}{\phi_{i,stress}^{q_i}} \tag{B.8}$$

where q_i is the Archie cementation index which can be experimentally obtained [75]. Similarly, in the initial state, we have the expressions of the initial tortuosity of medium i (τ_{i0}) and the initial pore size (r_{i0}):

$$\tau_{i0} = \frac{1}{\phi_{i0}^{q_i}} \tag{B.9}$$

$$r_{i0} = \sqrt{\frac{8k_{i0}\tau_{i0}}{\phi_{i0}}} \tag{B.10}$$

Comparing Eq. (B.7) and Eq. (B.10), then combining Eqs. (B.8) and (B.9), and applying the cubic law, we have:

$$r_{i,stress} = r_{i0}\cdot\left(\frac{\phi_{i,stress}}{\phi_{i0}}\right)^{1-0.5q_i} \tag{B.11}$$

Substituting Eq. (B.11) into Eq. (B.3) to obtain the final expression of Kn_i:

$$Kn_i = \frac{\mu_g}{4p_{gi}}\sqrt{\frac{\pi Z_i RT(\phi_{i0})^{1+q_i}}{Mk_{i0}}}\left(\frac{\phi_{i0}}{\phi_{i,stress}}\right)^{1-0.5q_i} \tag{B.12}$$

Similarly, the final expression of Kn_{i0} is:

$$Kn_{i0} = \frac{\mu_g}{4p_{gi0}}\sqrt{\frac{\pi Z_{i0} RT(\phi_{i0})^{1+q_i}}{Mk_{i0}}} \tag{B.13}$$

Thus, the obtained Kn_i and Kn_{i0} can be used to calculate the apparent permeabilities by Eq. and Eq., respectively.

Appendix C:. Capillary pressure and relative permeabilities in inorganic matrix, natural fractures network, and primary hydraulic fracture

For IM, NA, and HF, the capillary pressure p_{ci} ($i = m$ for IM, $i = na$ for NA, and $i = f$ for HF) is determined by using the analytical model proposed by Brooks and Corey [57]:

$$p_{ci} = p_{ei}\sqrt{\frac{1}{S_{wei}}} \tag{C.1}$$

where p_{ei} is the characteristic entry pressure of medium i; S_{wei} is the effective relative permeability of water in medium i, obtained by the following formula:

$$S_{wei} = \frac{S_{wi} - S_{wri}}{1 - S_{wri} - S_{gri}} \tag{C.2}$$

where S_{wi} is the water saturation in medium i; S_{wri} is the irreducible water saturation; S_{gri} is the irreducible gas saturation. Note that the values of S_{wri} and S_{gri} in IM, NA, and HF may be different due to the difference in fluid wettabilities and pore structures, as claimed in the previous studies [11,30].

The relative permeabilities of gas and water in medium i are determined by using the following expressions:

$$\begin{cases} k_{rgi} = (1 - S_{wei})^2\left[1 - S_{wei}^{(1+2/\chi)}\right] \\ k_{rwi} = S_{wei}^{(3+2/\chi)} \end{cases} \tag{C.3}$$

where k_{rgi} is the relative permeability of gas in medium i; k_{rwi} is the relative permeability of water in medium i; χ is a pore size distribution index, $\chi = 2$.

References

[1] Lee T, Bocquet L, Coasne B. Activated desorption at heterogeneous interfaces and long-time kinetics of hydrocarbon recovery from nanoporous media. Nat Commun 2016;7:11890. https://doi.org/10.1038/ncomms11890.

[2] Pan X, Zhang G, Chen J. The construction of shale rock physics model and brittleness prediction for high-porosity shale gas-bearing reservoir. Pet Sci 2020; 17:658–70. https://doi.org/10.1007/s12182-020-00432-2.

[3] Zhang Z, Liu Y, Sun H, Xiong W, Shen K, Ba Q. An alternative approach to match field production data from unconventional gas-bearing systems. Pet Sci 2020;17: 1370–88. https://doi.org/10.1007/s12182-020-00454-w.

[4] Li W, Liu J, Zeng J, Leong YK, Elsworth D, Tian J, et al. A fully coupled multidomain and multiphysics model for evaluation of shale gas extraction. Fuel 2020;278:118214. https://doi.org/10.1016/j.fuel.2020.118214.

[5] Zhang Q, Wang W, Kade Y, Wang B, Xiong L. Analysis of gas transport behavior in organic and inorganic nanopores based on a unified apparent gas permeability model. Pet Sci 2020;17:168–81. https://doi.org/10.1007/s12182-019-00358-4.

[6] Zeng J, Liu J, Li W, Leong YK, Elsworth D, Guo J. Shale gas reservoir modeling and production evaluation considering complex gas transport mechanisms and dispersed distribution of kerogen. Pet Sci 2021;18:195–218. https://doi.org/10.1007/s12182-020-00495-1.

[7] Rezaee R. Fundamentals of Gas Shale Reservoirs. 1st edition. New Jersey: John Wiley & Sons; 2015.

[8] Engelder, T., Cathles, L.M., Bryndzia., L.T., 2014. The fate of residual treatment water in gas shale. *Journal of Unconventional Oil and Gas Resources*. 1: 33–48. 10.1016/j.juogr.2014.03.002.

[9] Makhanov K, Habibi A, Dehghanpour H, Kuru E. Liquid uptake of gas shales: A workflow to estimate water loss during shut-in periods after fracturing operations. Journal of Unconventional Oil and Gas Resources 2014;7:22–32. https://doi.org/10.1016/j.juogr.2014.04.001.

[10] Shen W, Xu Y, Li X, Huang W, Gu J. Numerical simulation of gas and water flow mechanism in hydraulically fractured shale gas reservoirs. J Nat Gas Sci Eng 2016; 35:726–35. https://doi.org/10.1016/j.jngse.2016.08.078.

[11] Cheng Y. Impact of water dynamics in fractures on the performance of hydraulically fractured wells in gas-shale reservoirs. J Can Pet Technol 2012;51: 143–51. https://doi.org/10.2118/127863-PA.

[12] Wang H, Wang JG, Wang X, Dou F. Interaction of shale gas recovery and moisture transport in post two-phase flowback stage. J Nat Gas Sci Eng 2019;68:102897. https://doi.org/10.1016/j.jngse.2019.05.010.

[13] Thararoop P, Karpyn ZT, Ertekin T. Development of a multi-mechanistic, dual-porosity, dual-permeability, numerical flow model for coalbed methane reservoirs. J Nat Gas Sci Eng 2012;8:121–31. https://doi.org/10.1016/j.jngse.2012.01.004.

[14] Cao P, Liu J, Leong YK. A multiscale-multiphase simulation model for the evaluation of shale gas recovery coupled the effect of water flowback. Fuel 2017; 199:191–205. https://doi.org/10.1016/j.fuel.2017.02.078.

[15] Liu Y, Leung JY, Chalaturnyk RJ, Virues CJ. New insights on mechanisms controlling fracturing-fluid distribution and their effects on well performance in shale-gas reservoirs. SPE Prod Oper 2019;34:564–85. https://doi.org/10.2118/185043-PA.

[16] Chen Z, Huan G, Ma Y. Computational Methods for Multiphase Flows in Porous Media. 1st ed. Philadelphia: Society for Industrial and Applied Mathematics; 2006.

[17] Curtis JB. AAPG Bull 2002;86:1921–38. https://doi.org/10.1306/61EEDDBE-173E-11D7-8645000102C1865D.

[18] Ettinger, I.L., Lidin, G.D., Dmitriev, A.M., Shaupachina, E.S., 1958. *Systematic Handbook for the Determination of the Methane Content of Coal Seams From the Seam Pressure of the Gas and the Methane Capacity of the Coal*. U.S. Bureau of Mines Translation No. 1505/National Board Translation No. A.1606/SHE: Moscow.

[19] Crosdale PJ, Moore TA, Mares TE. Influence of moisture content and temperature on methane adsorption isotherm analysis for coals from a low-rank, biogenically-sourced gas reservoir. Int J Coal Geol 2008;76:166–74. https://doi.org/10.1016/j.coal.2008.04.004.

[20] Chen D, Pan Z, Liu J, Connell LD. Modeling and simulation of moisture effect on gas storage and transport in coal seams. Energy Fuels 2012;26:1695–706. https://doi.org/10.1021/ef2014327.

[21] Peng Y, Qu H, Liu J, Pan Z, Wu K, Dong X, et al. Impact of fluid adsorption on geomechanical properties of shale gas reservoir and shale gas recovery rate. Presented at the *52nd U.S. Rock Mechanics/Geomechanics Symposium*. 2018.

[22] Cui G, Tan Y, Chen T, Feng XT, Elsworth D, Pan Z, et al. Multidomain two-phase flow model to study the impacts of hydraulic fracturing on shale gas production. Energy Fuels 2020;34:4273–88. https://doi.org/10.1021/acs.energyfuels.0c00062.

[23] Cao P, Liu J, Leong YK. A fully coupled multiscale shale deformation-gas transport model for the evaluation of shale gas extraction. Fuel 2016;178:103–17. https://doi.org/10.1016/j.fuel.2016.03.055.

[24] Cao P, Liu J, Leong YK. General gas permeability model for porous media: Bridging the gaps between conventional and unconventional natural gas reservoirs. Energy Fuels 2016;30:5492–505. https://doi.org/10.1021/acs.energyfuels.6b00683.

[25] Li W, Liu J, Zeng J, Leong YK, Elsworth D. A fully coupled multidomain and multiphysics model for shale gas production. Presented at the *5th ISRM Young Scholars' Symposium on Rock Mechanics and International Symposium on Rock Engineering for Innovative Future*. 2019.

[26] Wei M, Liu J, Elsworth D, Wang E. Triple-porosity modelling for the simulation of multiscale flow mechanisms in shale reservoirs. Geofluids 2018;2018:6948726. https://doi.org/10.1155/2018/6948726.

[27] Civan F. Effective correlation of apparent gas permeability in tight porous media. Transp Porous Media 2010;82:375–84. https://doi.org/10.1007/s11242-009-9432-z.

[28] Wu K, Li X, Guo C, Wang C, Chen Z. A unified model for gas transfer in nanopores of shale-gas reservoirs: Coupling pore diffusion and surface diffusion. SPE J 2016; 21:1583–611. https://doi.org/10.2118/2014-1921039-PA.

[29] Chen Z, Liu J, Kabir A, Wang J, Pan Z. Impact of various parameters on the production of coalbed methane. SPE J 2013;18:910–23. https://doi.org/10.2118/162722-PA.

[30] Jurus, W.J., Whitson, C.H., Golan, M., 2013. Modeling water flow in hydraulically-fractured shale wells. Presented at the *SPE Annual Technical Conference and Exhibition*. New Orleans, Louisiana, September 30–October 2. 10.2118/166439-MS.

[31] Sang G, Elsworth D, Miao X, Mao X, Wang J. Numerical study of a stress dependent triple porosity model for shale gas reservoirs accommodating gas diffusion in kerogen. J Nat Gas Sci Eng 2016;32:423–38. https://doi.org/10.1016/j.jngse.2016.04.044.

[32] Wang K, Wang G, Jiang Y, Wang S, Han W, Chen X. How transport properties of a shale gas reservoir change during extraction: A strain-dependent triple-porosity model. J Nat Gas Sci Eng 2019;180:1088–100. https://doi.org/10.1016/j.petrol.2019.06.006.

[33] Detournay E, Cheng AHD. Fundamentals of Poroelasticity. Oxford: Pergamon 1993:113–71. https://doi.org/10.1016/B978-0-08-040615-2.50011-3.

[34] Zhang H, Liu J, Elsworth D. How sorption-induced matrix deformation affects gas flow in coal seams: A new FE model. Int J Rock Mech Min Sci 2008;45:1226–36. https://doi.org/10.1016/j.ijrmms.2007.11.007.

[35] Peng Y, Liu J, Pan Z, Connell LD. A sequential model of shale gas transport under the influence of fully coupled multiple processes. J Nat Gas Sci Eng 2015;27: 808–21. https://doi.org/10.1016/j.jngse.2015.09.031.

[36] Rutqvist J, Wu YS, Tsang CF, Bodvarsson G. A modeling approach for analysis of coupled multiphase fluid flow, heat transfer, and deformation in fractured porous rock. Int J Rock Mech Min Sci 2002;39:429–42. https://doi.org/10.1016/S1365-1609(02)00022-9.

[37] Li S, Fan C, Han J, Luo M, Yang Z, Bi H. A fully coupled thermal-hydraulic-mechanical model with two-phase flow for coalbed methane extraction. J Nat Gas Sci Eng 2016;33:324–36. https://doi.org/10.1016/j.jngse.2016.05.032.

[38] Berryman JG. Extension of poroelastic analysis to double-porosity materials: new technique in microgeomechanics. J Eng Mech 2002;128:840–7. https://doi.org/10.1061/(ASCE)0733-9399(2002)128:8(840).

[39] Mehrabian A, Abousleiman YN. Gassmann equations and the constitutive relations for multiple-porosity and multiple-permeability poroelasticity with applications to oil and gas shale. Int J Numer Anal Meth Geomech 2015;39:1547–69. https://doi.org/10.1002/nag.2399.

[40] Cui X, Bustin RM. Volumetric strain associated with methane desorption and its impact on coalbed gas production from deep coal seams. AAPG Bull 2005;89: 1181–202. https://doi.org/10.1306/05110504114.

[41] Palmer I, Mansoori J. How permeability depends on stress and pore pressure in coalbeds: A new model. SPE Reservoir Eval Eng 1998;1:539–44. https://doi.org/10.2118/52607-PA.

[42] Gu F, Chalaturnyk R. Permeability and porosity models considering anisotropy and discontinuity of coalbeds and application in coupled simulation. J Petrol Sci Eng 2010;74:113–31. https://doi.org/10.1016/j.petrol.2010.09.002.

[43] Kazemi H, Gilman JR, Elsharkawy AM. Analytical and numerical solution of oil recovery from fractured reservoirs with empirical transfer functions (includes associated papers 25528 and 25818). SPE Reservoir Eng 1992;7:219–27. https://doi.org/10.2118/19849-PA.

[44] Cassie ABD, Baxter S. Wettability of porous surfaces. Trans Faraday Soc 1944;40: 546–51. https://pubs.rsc.org/en/content/articlepdf/1944/tf/tf9444000546?casa_token=Lf_EXxhLlisAAAAA:W2A-fjFAb-XL-eQEK6V0l8WC4LQ8lA5TWeDdnQXVhX3iWH52n4nUzFT_X1H3GeNp7MkYCTwwAZjRrg.

[45] de Gennes PG. Wetting: statics and dynamics. Rev Mod Phys 1985;57:827–63. https://doi.org/10.1103/RevModPhys.57.827.

[46] Hibbe F, Chmelik C, Heinke L, Pramanik S, Li J, Ruthven DM, et al. The nature of surface barriers on nanoporous solids explored by microimaging of transient guest distributions. J Am Chem Soc 2011;133:2804–7. https://doi.org/10.1021/ja108625z.

[47] Kärger J, Binder T, Chmelik C, Hibbe F, Krautscheid H, Krishna R, et al. Microimaging of transient guest profiles to monitor mass transfer in nanoporous materials. Nat Mater 2014;13:333–43. https://doi.org/10.1038/nmat3917.

[48] Xue Y, Markmann J, Duan H, Weissmüller J, Huber P. Switchable imbibition in nanoporous gold. Nat Commun 2014;5:1–8. https://doi.org/10.1038/ncomms5237.

[49] Huber P. Soft matter in hard confinement: phase transition thermodynamics, structure, texture, diffusion and flow in nanoporous media. J Phys: Condens Matter 2015;27(10):103102.

[50] Drew M. Surfaces, interfaces and colloids. 4th ed. New York: Wiley-VCH; 1999.

[51] Li W, Zhao X, Li Y, Ji Y, Peng H, Liu L, et al. Laboratory investigations on the effects of surfactants on rate of penetration in rotary diamond drilling. J Petrol Sci Eng 2015;134:114–22. https://doi.org/10.1016/j.petrol.2015.07.027.

[52] Mirchi V, Saraji S, Goual L, Piri M. Dynamic interfacial tension and wettability of shale in the presence of surfactants at reservoir conditions. Fuel 2015;148:127–38. https://doi.org/10.1016/j.advwatres.2021.103964.

[53] Hashemi L, Glerum W, Farajzadeh R, Hajibeygi H. Contact angle measurement for hydrogen/brine/sandstone system using captive-bubble method relevant for underground hydrogen storage. Adv Water Resour 2021;154:103964. https://doi.org/10.1016/j.advwatres.2021.103964.

[54] Ren QY, Chen GJ, Yan W, Guo TM. Interfacial tension of (CO_2 + CH_4) + water from 298 K to 373 K and pressures up to 30 MPa. J Chem Eng Data 2000;45:610–2. https://doi.org/10.1021/je990301s.
[55] Song XG, Zhao MW, Dai CL, Wang XK, Lv WJ. Mechanism of active silica nanofluids based on interface-regulated effect during spontaneous imbibition. Pet Sci 2021;18:883–94.
[56] Chavent G, Jaffre J. Mathematical Models and Finite Elements for Reservoir Simulation: Single Phase, Multiphase and Multicomponent Flows through Porous Media. 1st ed. Amsterdam: Elsevier Science Publishers B.V; 1986.
[57] Brooks RH, Corey AT. Hydraulic properties of porous media and their relation to drainage design. Hydrology Papers, Colorado State University 1964;24:37. https://www.wipp.energy.gov/information_repository/cra/CRA-2014/References/Others/Brooks_Corey_1964_Hydraulic_Properties_ERMS241117.pdf.
[58] Wang F, Pan Z, Zhang Y, Zhang S. Simulation of coupled hydro-mechanical-chemical phenomena in hydraulically fractured gas shale during fracturing-fluid flowback. J Petrol Sci Eng 2018;163:16–26. https://doi.org/10.1016/j.petrol.2017.12.029.
[59] Brown PN, Hindmarsh AC, Petzold LR. Using Krylov methods in the solution of large-scale differential-algebraic systems. SIAM Journal on Scientific Computing 1994;15:1467–88. https://doi.org/10.1137/0915088.
[60] Hindmarsh AC, Brown PN, Grant KE, Lee SL, Serban R, Shumaker DE, et al. SUNDIALS: Suite of nonlinear and differential/algebraic equation solvers. ACM Transactions on Mathematical Software (TOMS) 2005;31:363–96. https://doi.org/10.1145/1089014.1089020.
[61] COMSOL, A.B., 2019. *COMSOL multiphysics reference manual, Version 5.5*. COMSOL AB: 1300.
[62] Al-Ahmadi, H.A., Wattenbarger, R.A., 2011. Triple-porosity models: one further step towards capturing fractured reservoirs heterogeneity. Presented at the *SPE/DGS Saudi Arabia Section Technical Symposium and Exhibition*, Al-Khobar, Saudi Arabia, May 15–18. 10.2118/149054-MS.
[63] Shaoul J, van Zelm L, de Pater CJ. Damage mechanisms in unconventional-gas-well stimulation—A new look at an old problem. SPE Prod Oper 2011;26:388–400. https://doi.org/10.2118/142479-PA.
[64] Wang H, Wang JG, Gao F, Wang X. A two-phase flowback model for multiscale diffusion and flow in fractured shale gas reservoirs. Geofluids 2018;2018:5910437. https://doi.org/10.1155/2018/5910437.
[65] Sakhaee-Pour A, Bryant S. Gas permeability of shale. SPE Reservoir Eval Eng 2012;15:401–9. https://doi.org/10.2118/146944-PA.
[66] Brant Bennion D. An overview of formation damage mechanisms causing a reduction in the productivity and injectivity of oil and gas producing formations. J Can Pet Technol 2002;41:29–36. https://doi.org/10.2118/02-11-DAS.
[67] Li W, Liu J, Zhao X, Yang C, Zhang J, Li Y, et al. Effect of flushing fluid composition on rate of penetration in limestone: Surface and interface aspects. Presented at the *ISRM 1st International Conference on Advances in Rock Mechanics - TuniRock 2018*. 2018.
[68] Al-Muntasheri GA. A critical review of hydraulic-fracturing fluids for moderate- to ultralow-permeability formations over the last decade. SPE Prod Oper 2014;29:243–60. https://doi.org/10.2118/169552-PA.
[69] Li W, Liu J, Zeng J, Tian J, Li L, Zhang M, et al. A critical review of the application of nanomaterials in frac fluids. In: The state of the art and challenges. Presented at the *SPE Middle East Oil and Gas Show and Conference*; 2019. https://doi.org/10.2118/195029-MS.
[70] Cao Y, Zhang J, Zhai H, Fu G, Tian L, Liu S. CO_2 gas fracturing: A novel reservoir stimulation technology in low permeability gassy coal seams. Fuel 2017;203:197–207. https://doi.org/10.1016/j.fuel.2017.04.053.
[71] Mahmoud M. Development of a new correlation of gas compressibility factor (Z-factor) for high pressure gas reservoirs. Journal of Energy Resources and Technology 2014;136:012903. https://doi.org/10.1115/1.4025019.
[72] Beskok A, Karniadakis GE. Report: A model for flows in channels, pipes, and ducts at micro and nano scales. Microscale Thermophys Eng 1999;3:43–77. https://doi.org/10.1080/108939599199864.
[73] Civan F, Rai CS, Sondergeld CH. Shale-gas permeability and diffusivity inferred by improved formulation of relevant retention and transport mechanisms. Transp Porous Media 2011;86:925–44. https://doi.org/10.1007/s11242-010-9665-x.
[74] Civan F, Rai CS, Sondergeld CH. Determining shale permeability to gas by simultaneous analysis of various pressure tests. SPE J 2012;17:717–26. https://doi.org/10.2118/144253-PA.
[75] Iversen N, Jorgensen BB. Diffusion coefficients of sulfate and methane in marine sediment: Influence of porosity. Geochim Cosmochim Acta 1993;57:571–8. https://doi.org/10.1016/0016-7037(93)90368-7.